Towards an understanding of the SEI formation and lithium preferential plating on copper

Svetlana Menkin[1], Christopher A. O'Keefe[1], Anna B. Gunnarsdóttir[1], Sunita Dey[1], Federico Pesci[2], Zonghao Shen[2], Ainara Aguadero[2], Clare P. Grey[1]

1. Department of Chemistry, University of Cambridge, Lensfield Road, Cambridge, CB2 1EW
2. Department of Materials, Imperial College London, Royal School of Mines, SW7 2AZ

Abstract

'Anode-free' batteries present a significant advantage due to their substantially higher energy density and ease of assembly in a dry air atmosphere. However, potential safety issues due to lithium (Li) dendrite growth rather than smooth Li metal plating on the Cu current collector, and low cycling coulombic efficiency during their operation are delaying their practical implementation. To understand the interplay between Cu surface chemistry and the morphology of the plated Li, we studied the SEI formation on Cu and the preferential plating of Li using ssNMR, *insitu* NMR, XPS, ToF-SIMS, SEM and EIS.

A native interphase layer (N-SEI) is formed instantaneously on copper current collectors upon their immersion in $LiPF_6$-based electrolyte. The nature of the N-SEI is affected by the copper interface composition, homogeneity and formation time. In addition to the typical SEI components, it contains Cu_xO and its reaction products. Parasitic semi-reversible electrochemical reactions were observed with *in-situ* NMR measurements of Li plating efficiency during the first five cycles. The morphology of the plated lithium is affected by the SEI homogeneity, current density and rest time in the electrolyte before the plating. The preferential plating of Li is governed by the distribution of ionic conducting compounds rather than electronic conducting compounds.

Introduction

The strive for higher energy density for rechargeable lithium (Li) batteries has created a renaissance of interest in Li-metal anodes. Yet, Li metal secondary batteries are disadvantaged by multiple safety issues, rendering this class of batteries potentially unsafe and impractical owing to the risk of thermal runaway.

Recent studies suggest that the use of excessive thickness of Li metal in full battery cells promotes fast cell degradation, decreases the practical energy density and increases safety concerns. [1] 'Anode-free' or 'Li free' batteries are aimed to address these challenges. 'Anode-free' cells are composed of a Li-ion cathode and a thin layer of Li metal that is electroplated

on the copper (Cu) current collector during charging. These types of batteries present a significant advantage due to their higher energy density, ease of assembly in a dry air atmosphere and improved sustainability. However, potential safety issues due to Li dendrite growth and low cycling coulombic efficiency are delaying their practical implementation. [2–4]

The solid-electrolyte interphase (SEI) is the key factor which determines the performance and safety of Li metal batteries. It serves as an interphase between the metal and the electrolyte and has the properties of a composite solid electrolyte. [5,6] It has been widely demonstrated in the literature that non-homogeneous SEI compositions and morphologies initiate uneven plating and stripping of Li metal anodes, resulting in dendritic short circuits.[1,7,8]

The SEI on the Cu current collector further reacts when current is passed, prior to the Li plating, and this is termed the electrochemical SEI (e-SEI) in this study. The existing studies of the SEI formed on Cu suggest a different SEI chemical composition compared to the SEI formed on Li metal anodes. [3,9–12] Schmitz et al.[4] found that the SEI on electrodeposited Li on Cu was composed of Li carbide (Li_2C_2) and Li carbonate (Li_2CO_3), the former being primarily present on Li deposits and the latter more homogeneously distributed. Guidotti et al.[13] found significant concentration of CuF_2 in the SEI on Cu. Kitz et al.[10] studied the SEI on Cu and concluded that multiple faradaic processes occur between 3 V and 1.5 V vs. Li metal, resulting in the formation of a dense primary SEI composed of Li_2O, OH^- (or alkoxide), LiF, polyethylene glycol and Cu nanoparticles on the exposed Cu surface. Interestingly, LiF is formed on Cu as a result of electrocatalytic reduction of HF at 2 V on the Cu surface, while the same reaction occurs at lower potentials on the traditional graphite anode (~0.25 V). [10,14]

Li plating mechanisms and SEI formation have been extensively studied with electrochemical impedance spectroscopy (EIS), X-ray photoelectron spectroscopy (XPS), Time-of-Flight Secondary Ion Mass Spectrometry (ToF-SIMS), electrochemical quartz crystal microbalance (EQCM), scanning and tunneling electron microscopy (SEM and TEM). [10,15–18] However, it is remains challenging to estimate the effect of the current collector, separate the capacity of the plated Li from parasitic reactions and SEI formation reactions, and to assign the chemical and electrochemical reaction products to specific SEI formation stages. The study of these phenomena is essential for the understanding of the Li metal anode cycling mechanism on Cu and the development of high-energy, long-life and safe ‘anode free’ batteries.

The native surface oxide film on alkali metal anodes is commonly referred to as a native SEI (N-SEI). Here the definition of N-SEI is expanded to the surface passivation layer on the Cu

current collector, which is already present on Cu, but which is modified by the further spontaneous reactions that occur upon immersion in an electrolyte. In the system under study, the main product of the N-SEI is LiF from the decomposition of $LiFP_6$.

This paper reports the effect of the surface chemistry of the Cu current collector on the chemical composition of the SEI and the plating of Li metal. The results section will follow the formation process of the SEI on Cu and Li plating: the N-SEI formation, the e-SEI formation and Li plating. The effect of the Cu surface treatment and the corresponding Cu oxide layer on the N-SEI is studied by EIS, XPS and solid-state NMR (ssNMR) spectroscopy. The e-SEI, generated by a prolonged constant voltage hold, is studied to isolate the SEI composition at different potentials on the SEI formation curve (Figure 1). The voltage hold was performed at potentials typical for Cu oxide reduction and lithiation potentials [19–25] and characteristic SEI formation potentials in $LiPF_6$ based electrolyte.[17,26]

A typical preparation procedure for Cu current collectors in the literature is the pre-treatment by dilute hydrochloric acid treated (the current collectors being termed d-HCl-Cu in this study). [27,28] The d-HCl surface treatment and the corresponding SEI that forms was compared to the SEI on Cu pre-treated by concentrated acetic acid (c-AcH-Cu). The c-AcH surface treatments have been reported to give rise to a thicker and more homogeneous Cu oxide surface layers. [29]

We show with ssNMR and EIS that a native interphase (N-SEI) is formed instantaneously on Cu current collectors upon their immersion in $LiPF_6$ -based electrolytes. *In situ* NMR measurements were used to track Li metal deposition in a Cu – $LiFePO_4$ (LFP) cell. Parasitic semi-reversible electrochemical reactions occur in the course of the first five cycles in a cell with d-HCl-Cu. Thus, the Li plating efficiency on d-HCl-Cu is lower than measured electrochemically. The morphology of the plated Li and efficiency of the Li plating-stripping process was shown to depend on the homogeneity of the Cu oxide layer and N-SEI on Cu. The preferential plating of Li, dictated by the local composition of the SEI and its ionic conductivity, was demonstrated by ToF-SIMS and XPS.

Experimental

Materials The electrolyte used was 1 M $LiPF_6$ in 1:1 v/v ethylene carbonate/dimethyl carbonate (EC/DMC; Sigma Aldrich battery grade, LP30). In all the coin cells, pre-cut Li metal disks (LTS research, 99.95%) were used. The materials were stored and handled in an Ar atmosphere glovebox (O_2, H_2O < 1 ppm, MBraun). Cu metal foil (MTI) was used as a substrate

for Li plating. Cu metal flakes (average particle size of 0.4 mm, Aldrich), CuO (<50 nm, Aldrich) and Cu_2O (<350 nm, Aldrich) were used as Cu/Cu_xO substrates for N-SEI samples for ssNMR experiments. Acetic acid (Fischer Chemical; Lab reagent grade, glacial) was used as received. Hydrochloric acid (Honeywell, Fluka, (07102)) was diluted to 1.1 M in deionized water. The water content in the electrolyte was 10-30 ppm (measured with Karl Fischer titration, Metrohm). Polypropylene-polyethylene (PPPE) (Celgard) and glass fiber (Whatman) separators were dried under vacuum at 40 ºC and 100 ºC, respectively.

Current collector pretreatment Cu metal disks and Cu metal flakes were soaked in either concentrated acetic acid (denoted c-AcH-Cu) or dilute hydrochloric acid (denoted d-HCl-Cu) for 10 minutes for surface oxide removal. The d-HCl treated Cu was afterwards rinsed with acetone. Following a previously reported surface treatment, the c-AcH-Cu the acid was removed with a dry nitrogen flow. The disks were then dried at 100 °C under vacuum overnight.[29]

Cell Fabrication Symmetric cells, composed of two pre-treated Cu current collectors (thickness 25 µm), and Cu-Li half cells were assembled in coin cells (Cambridge Energy Solutions) with three stainless steel disks (thickness 0.5 mm) and 75 µL of LP30 electrolyte.

The *in situ* NMR cell were assembled in a capsule cell (NMR Service) made out of polyether ether ketone (PEEK) as described previously. [30] $LiFePO_4$ (LFP) cathodes (MTI) were casted on carbon coated Al foil and copper foils (to be used as anode current collectors) were cut into approximately 0.4 cm^2 rectangular electrodes. Slightly larger rectangular PPPE and glass fiber separators were sandwiched between the LFP cathode and Cu, with the PPPE facing the Cu. The volume of 100 µl LP30 electrolyte was used.

Electrochemistry N-SEI was formed during the cell storage prior to e-SEI formation and Li plating. e-SEI was formed at constant voltages of 2, 1.4 and 0.1 V. Positive constant voltage was applied on Li-Cu coin cell for 2 to 24 hours. Li plating was done at a constant current in the range of 0.03-1.2 $mAcm^{-2}$ after rest times of 0 to 12 hours (a typical deposition curve is depicted in Figure 1). For the ToF-SIMS and XPS studies of Li preferential plating, thin (0.1 mAh) Li nucleation layers were plated on the Cu at 0.065 $mAcm^{-2}$ current density. Potentiostatic Impedance spectroscopy (PEIS) experiments were conducted in the 1 MHz – 1 Hz frequency range, with an amplitude of 10 mV.

Sample preparation and transfer

For the preparation of the native N-SEI on Cu samples for ssNMR, Cu metal flakes or Cu oxide powders were soaked in the electrolyte either with or without the presence of metal Li and sealed in a coin cell inside the glovebox and left for variable periods of times ranging from 1 to 96 hours.

The SEI samples for ssNMR were prepared by scraping the plated Li metal gently from the Cu surface. The samples were mixed with ground KBr (dried at vacuum at 200 °C for 48 hours) and packed in a 2.5 mm zirconia rotor. For the SEM, XPS and ToF-SIMS, the samples (deposited on Cu disks) were mounted in an air-tight transfer module stage. The samples were left standing under vacuum in the glovebox antechamber for approximately 15 minutes in order to allow the DMC to evaporate prior to sample packing.

NMR The ssNMR experiments were conducted on a Bruker Avance III 500 MHz spectrometer using a 2.5 mm double channel Bruker MAS probe. ^{19}F and ^{7}Li chemical shifts were referenced externally using LiF as a secondary reference ($\delta_{iso}(^{19}F)$ = –204 ppm and $\delta_{iso}(^{7}Li)$ = –1 ppm). Magic angle spinning (MAS) up to 30 kHz was applied. The ^{19}F and ^{7}Li ssNMR was conducted using a rotor-synchronized Hahn echo pulse experiment with optimized 90° pulse lengths of 2.7 μs (^{19}F) and 3.3 μs (^{7}Li), with 5 and 1 second recycle delays for ^{19}F and ^{7}Li, respectively.

The *in-situ* NMR experiments were conducted on a Bruker Avance 300 MHz spectrometer (the respective Larmor frequency for ^{7}Li being 116.6 MHz). The spectra were recorded using an *in situ* ATMC probe (NMR Service) which contains leads to connect a battery positioned inside a solenoidal Ag-coated Cu coil to the potentiostat for battery cycling. The chemical shift of ^{7}Li was referenced to 1 M LiCl in water at 0 ppm. Single-pulse experiments were used to collect the NMR data, with a recycle delay of 1 s (T_1 for Li metal ~ 100 ms) and 256 transients were recorded. This resulted in an experimental time of about 4.5 minutes. The spectra were processed in Bruker Topspin software, using the automatic phase and baseline correction. Further data processing was done in R.

SEM SEM images were taken with a Tescan MIRA3 FEG-SEM instrument at an acceleration voltage of 5.0 kV. The electrodes were not rinsed with solvent but mounted onto the SEM stage of the transfer module (Kammrath & Weiss, type CT0). The samples were transferred into the

SEM chamber in the transfer module under the inert Ar atmosphere of the glove box a, without being exposed to air.

XPS A Thermo Scientific K-Alpha XPS system with a monochromated microfocused Al-Kα X-ray source (hν of 1468.7 eV) was used at a power of 72 W (12 kV x 6 mA). Samples were adhered to an airtight transfer chamber (Themo Fisher Scientific, sample area 60 X 60 mm) equipped with X-ray-transparent windows and were brought down to a measurement pressure of 10^{-8} mbar. The spot size of measurement was 200 µm with step size of 5 µm. Along with the high-resolution survey scan, element specific energy scans were recorded (step size 0.1 eV/min). Spectra were recorded after 10 and 20 nm sputtering (sputtering rate of 0.5 nm/sec) with an EX06 monoatomic Ar ion source (MAGCIS) of energy 2 keV. Data processing including background correction (Shirley function) and peak fitting (Gaussian-Lorentzian functions) were performed using the CasaXPS software (version 2.3.15). The C 1s photoelectron peak position of 284.8 eV was used as an internal reference for calibrating the spectra in order to nullify the effects of surface charging.

Secondary Ion Mass Spectrometry (SIMS) analysis was performed on a Time-of-Flight (ToF) SIMS 5 spectrometer (ION-TOF GmbH, Münster, Germany). The measurements were conducted in the burst alignment mode (BAM) for better lateral resolution of images with a Bi^+ primary beam (25 keV) and a Cs^+ sputtering beam (500 eV) over an area of 250 µm × 250 µm (sputtering area 500 µm × 500 µm). Additionally, for data analysis, the intensity of the species for different samples were all point-to-point normalized to the total counts and 3D reconstruction was also performed by using the Surfacelab 6.0 software in order to obtain the distribution of different species.

Results

Electrochemistry: To study the effect of the Cu oxide layer composition on Li metal plating, two different oxide removal procedures[29] were used to remove the inhomogeneous oxide-hydroxide layer on the untreated Cu metal, as described in the experimental section. A typical Li deposition curve of galvanostatic plating for Cu-Li half cells is shown in Figure 1, for the two Cu surface treatments d-HCl-Cu and c-AcH-Cu. The N-SEI is formed during the rest period at open circuit voltage (OCV). Once current is applied, e-SEI is formed by simultaneous decomposition and reduction of the electrolyte. When the Cu electrode reaches negative potential, Li metal is plated between the SEI and the Cu (Figure 1). The OCV values fluctuate around 2.8±0.4V for both surface treatments. The observed wide distribution between the cells

indicates that N-SEI formation processes are dynamic and very sensitive to both surface chemistry and cell assembly. The difference in the OCV could be due to variation in the copper oxide and copper fluoride layers on the Cu surface and the spontaneous formation of the N-SEI passivation layer. [25]

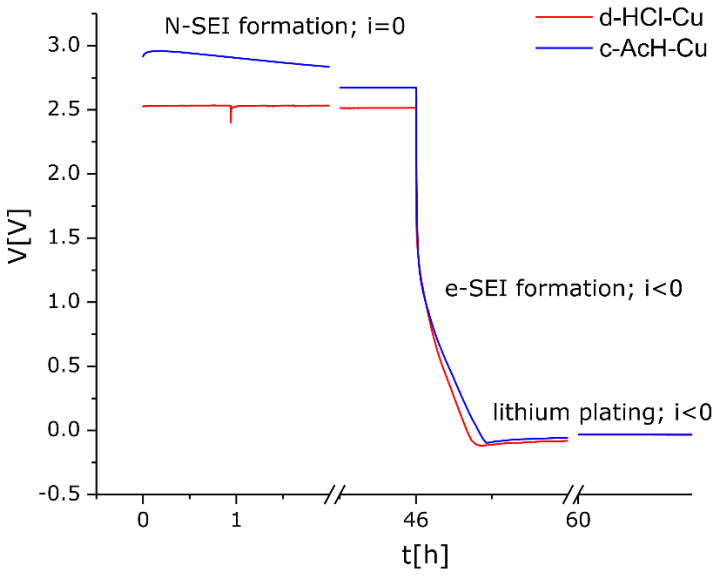

Figure 1. A typical response for a galvanostatic SEI formation and lithium deposition on copper using 0.03 mA/cm^2 current density (normalized for the Cu WE area) in a Cu-Li half-cell.

To explore the properties of the N-SEI, impedance measurements were performed on Cu-Cu symmetric cells as function of time, starting 1 hour after the cell assembly (Figure 2). The EIS Nyquist plot of d-HCl-Cu symmetrical cells is typical for a linear restricted diffusion towards a blocking electrode (Figure 2a).[31] In contrast, the Nyquist plot of a c-AcH-Cu symmetric cell (Figure 2b) was fitted with Voigt-type equivalent circuit (which includes at least one resistor-capacitor (RC) unit), typically assigned to surface films. [31] This could be the result of either more homogeneous passivation by Cu(II) oxide, as was demonstrated to be present on c-AcH-Cu by XPS (as described in the following XPS analysis, Figure 4), or due to the formation of a more dense N-SEI.

After 5-days' rest time, the fit of the impedance spectrum Nyquist plot for c-AcH-Cu required an additional RC component, assigned to the SEI. The diameter of the high-frequency semicircle, assigned to the compact surface films adjacent to the metal surface, decreases with time, while the total impedance has not changed significantly. The slope of the Nyquist plot of d-HCl-Cu decrease with time. This indicates a relative increase in the time constants of the

diffusional as compared to the faradaic processes.[32] We attribute these trends to an increase in the heterogeneity of the SEI after prolong rest time (see SI for detailed EIS analysis, Figures S1-2). [33,34]

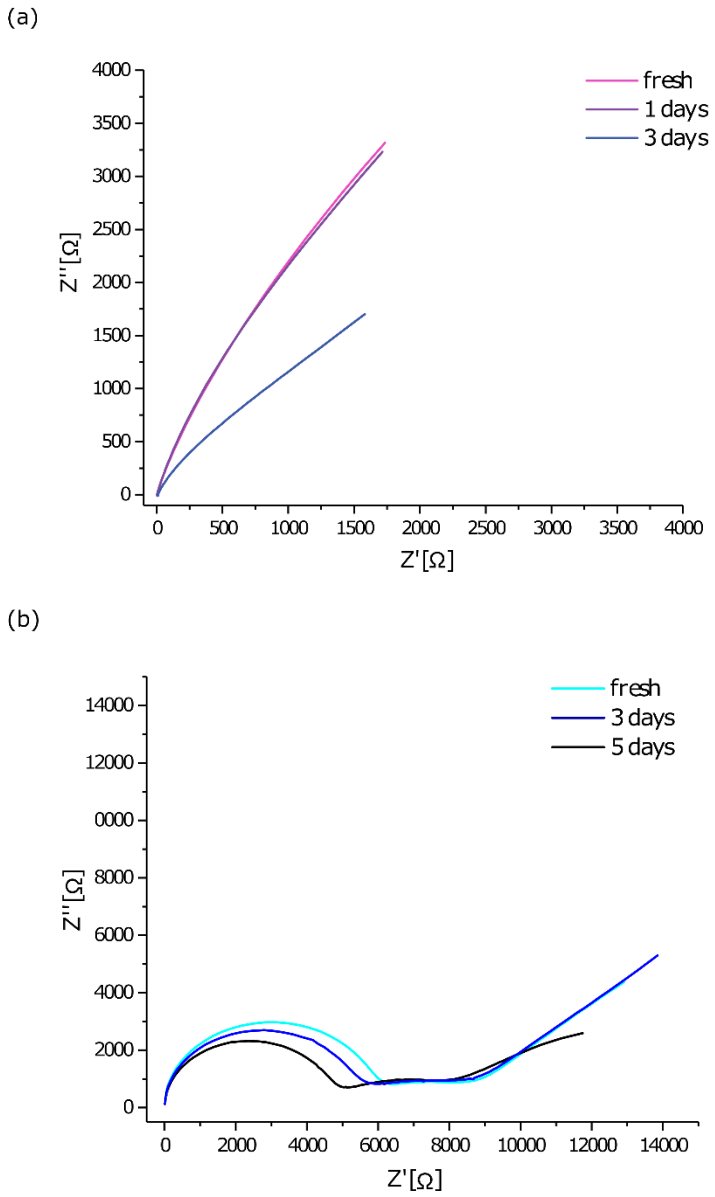

Figure 2. Nyquist plot of Cu-Cu symmetric cells of d-HCl-Cu(a) and c-AcH-Cu (b) foils performed with PEIS in the 1 MHz – 1 Hz frequency range, with an amplitude of 10 mV around the OCV.

Cyclic voltammogram (CV) of the first cycle of Li plating on c-AcH-Cu and d-HCl-Cu was measured in a three-electrode cell in the potential range of OCV to -0.2 V vs. Li at a 1 mV/s scan rate (Figure 3). The CV shows reduction peaks in three main voltage ranges. The peaks in the range of 2.5-3.1 V (area 1) are assigned to CuF_2 reduction, which results in LiF and Cu

formation (reaction 1). [19,35] Interestingly, the intensity of these peaks is lower on d-HCl-Cu (Figure 3b, red).

(1) $2Li^+ + CuF_2 \leftrightarrow Cu + 2LiF$

The peaks around 2.3-1.3 V (area 2) are attributed to Cu oxide reduction and its accompanying reactions. The areas of the peaks around 2 V for d-HCl-Cu are larger (Figure 3). The partially reversible peaks from 0.4 to -0.2 V (area 3, Figure 3a) are assigned to parasitic reactions, SEI formation and Li plating (reduction at negative potentials) and stripping (oxidation). The reversible peaks around 0.4V – 1 V and Li plating peaks remained for nine cycles (see CV for cycle 2 and 10 in Figure S25 in the SI).

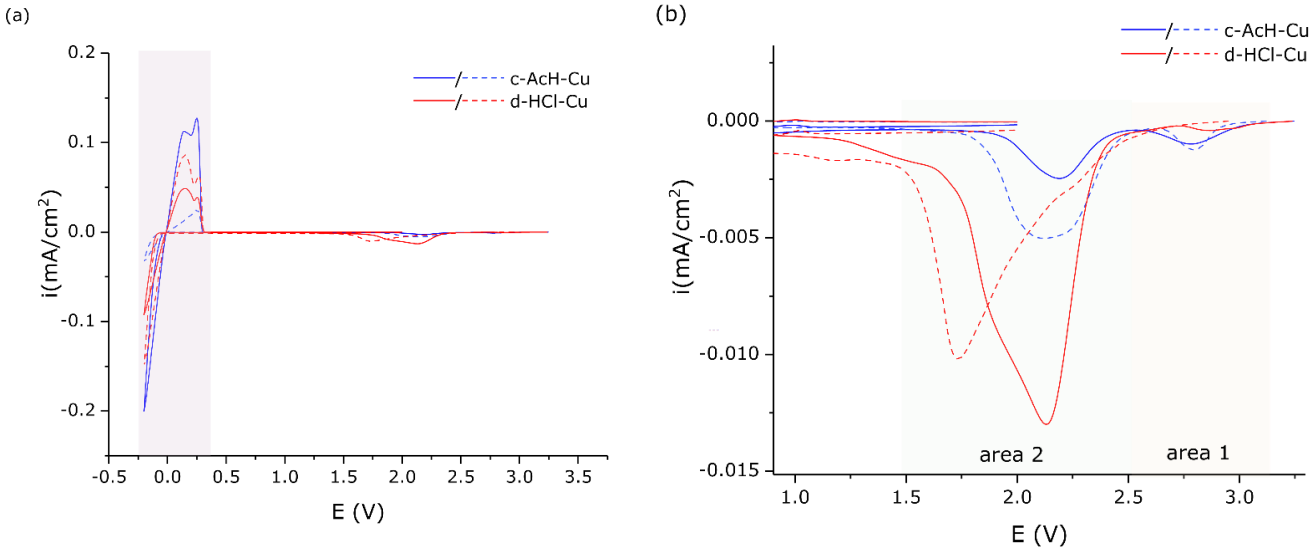

Figure 3. (a) 1st cycle CV of lithium plating on c-AcH-Cu (blue) and d-HCl-Cu (red) in three-electrode cell, Cu WE vs. Li disk CE and RE, with scan rate 1mV/sec (full line -sample 1, dashed line -sample 2). (b) Zoom-ed in view of the CV in (a), indicating the potential ranges of interest.

XPS: The surface of d-HCl-Cu and c-AcH-Cu foils was studied by XPS (Figure 4). The Auger Cu metal peaks (565 eV, 568 eV and 572 eV)[36,37], exclusive to the spectrum of d-HCl-Cu, indicate bare areas with thinner or no N-SEI and serve as evidence for the more heterogeneous surface of the oxide layer on d-HCl-Cu, compared to c-AcH-Cu and pristine non-treated Cu metal (Figure 4a). The peaks at 931-932.4 eV (Cu $2p_{3/2}$) and 951.9-952.2 eV (Cu $2p_{1/2}$), observed in the Cu 2p spectra (Figure 4b) and the O 1s peak at 530.2 eV (Figure S13 in the SI) are assigned to Cu metal and Cu(I) copper oxides. The shoulder observed in the Cu 2p spectra of c-AcH-Cu and the pristine copper current collector at 934-935 eV, the minor shake-up feature at 941-945 eV and the 531-531.2 eV peaks in the O 1s spectrum (Figure 4b, Figure S13

in the SI) serve as an indication for the presence of Cu(II) compounds, likely to be Cu(II) hydroxide.

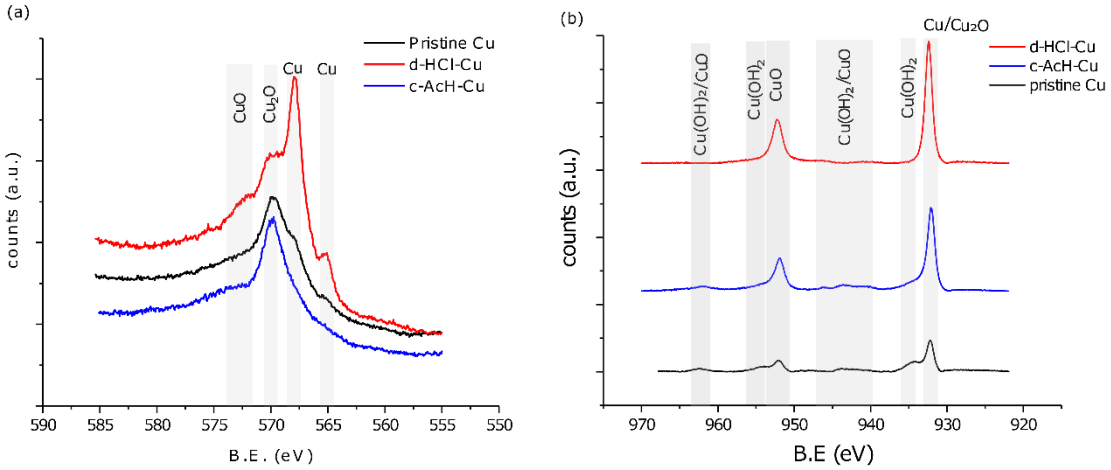

Figure 4. Auger spectra (a) and Cu 2p XPS spectra (b) of Cu pristine (black), d-HCl-Cu (red) and c-AcH-Cu (blue).

Consistent with the ^{19}F NMR, the XPS analysis of the N-SEI suggest that it is composed of Cu oxides (see SI for detailed XPS analysis, Figures S13-S14) and $LiPF_6$ decomposition products (Figure S16). As the SEI has a heterogeneous composition and thickness, the e-SEI intermixes with N-SEI that already formed prior to polarization. The 1.4 V SEI ($eSEI_{1.4}$) is dominated by the formation of C-O species as evident by the intense XPS C1s and O1s peaks at 286.6 eV and 533.4 eV, respectively (Figures S16 and S16b). Sputtering of approximately 10 nm revealed an increased C1s C-C/C-H peak intensity (around 284.4 eV); while additional peaks arise at C1s 289.7 eV and O1s 532.5 eV (Figure S18). These findings could be attributed to the formation of short and medium length PEO-like polymeric species on the surface and Li carbonate in the inner plane of the e-$SEI_{1.4V}$. [17,38,39] Similar polymeric species were observed on electrochemical SEI formed by the prolonged constant application of 2V (e-SEI_{2V}) (see detailed analysis in the SI, Figures S16-18).

The F1s XPS spectrum of the e-$SEI_{1.4V}$ shows that the signal attributed to LiF is significantly less dominant compared to those of N-SEI and e-SEI_{2V} (Figures S16c and S19). Sputtering of 20 nm (of e-$SEI_{1.4V}$) revealed nearly threefold increase in LiF:$LiPF_6$ ratio in comparison to the surface (Figure S18 and Table 2). Thus, LiF is mostly found in the inner plane of the e-$SEI_{1.4V}$, LiF formation occurs mostly during rest and at voltages above 1.4 V.

NMR: The N-SEI and e-SEI on Cu were studied by ^{19}F and ^{7}Li ssNMR under magic-angle spinning (MAS) conditions (Figure 5a). To increase the signal-to-noise in the ssNMR and mimic the N-SEI, acid-treated Cu metal flakes were soaked in the LP30 electrolyte, dried and packed into the MAS rotors. MAS of metallic samples is challenging as the rotation in a magnetic field induces eddy currents that results in unstable spinning. To alleviate this issue, samples were diluted with dry KBr prior to packing. In Figure 5, the ^{19}F NMR spectra for N-SEI on Li metal and d-HCl-Cu soaked in LP30 electrolyte are compared to that of the dried LP30 electrolyte mixed with KBr. For the Li and Cu samples, two groups of resonances between -72 and -85 ppm and between -202 and -204 ppm were observed. The first group of resonances is assigned to $LiPF_6$ salt and its decomposition products and the second to LiF.[40,41] The spontaneous formation of LiF was also observed in the ^{19}F NMR spectra of Cu oxides (Cu_2O and CuO) powders soaked in LP30 electrolyte (Figure S3).

As shown in Figure 5c, only signals corresponding to $LiPF_6$ were observed for the solidified electrolyte in dried KBr, indicating that the generation of LiF results from the reaction of the electrolyte on the metals surface and is not due to decomposition of the bulk electrolyte (according to reaction 1) or a reaction with the KBr. This indicates that the fluorine containing N-SEI can form upon soaking the metals and oxides in an electrolyte without any applied potential.

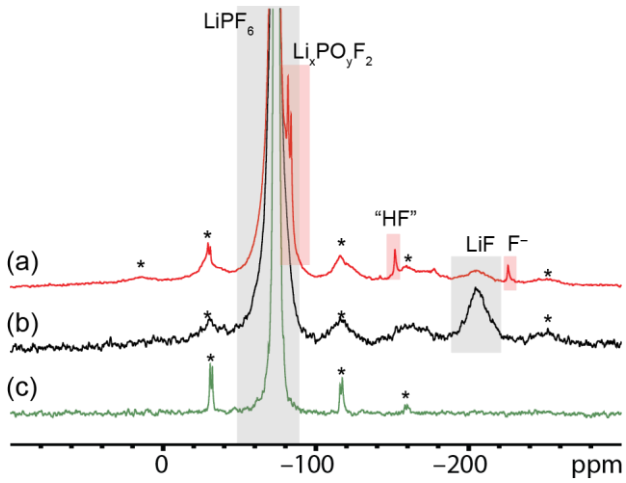

Figure 5. ^{19}F ssNMR spectra of (a) d-HCl -Cu flakes soaked in LP30 for 1 hour, (b) Li metal soaked in LP30 for 1 hour and (c) 75 µl of LP30 mixed with KBr and dried. The spectra were acquired with a MAS frequency of 20 kHz. Spinning sidebands are denoted with asterisks.

The resonance at -225 ppm is unique to soaked Cu samples, i.e. N-SEI on Cu (see Figure 5a, and Figures S3-5). There is no obvious assignment to this resonance: it is usually assigned to NaF, however NaF was not seen with ^{23}Na ssNMR on the studied samples.

To compare the N-SEIs on d-HCl-Cu and c-AcH-Cu, c-AcH-Cu flakes were soaked in LP30 for 1-24 hours (Figures S4-S5) and studied with ssNMR. The sample soaked for 24 hours had additional sharp resonances around -131, -142, -151, -170, and -184 ppm (Figure S5). This demonstrates that the formation of the N-SEI and the decomposition of the $LiPF_6$ salt is a dynamic process that is highly dependent on the Cu surface chemistry and soaking time (see detailed discussion on ^{19}F NMR of e-SEI_{2V} e-$SEI_{1.4V}$ in the SI, Figure S4-10).

The ^{7}Li NMR spectra for N-SEI on Cu flakes consist of single, relatively broad resonance in the range of 10 ppm to -10 ppm (Figures 6 and Figure S6) and corresponds to various diamagnetic Li-containing species within the SEI.[40] The ^{7}Li resonance for the short soaking time (1 hour) of c-AcH-Cu is significantly broader compared to that for long soaking time (18 hours) (Figure 6). However, for d-HCl-Cu, this trend is less significant (Figure S6). The resonances on all N-SEI were fitted with the combination of a broad and a narrow component, both have approximately the same shift (Figure S7). The resonance narrowing could be due to the formation of more mobile Li species or a decrease of the variety of Li compounds.[42] Interestingly, the deconvolution of the ^{7}Li resonance did not require the inclusion of a peak at -3 ppm (the typical shift of the $LiFP_6$ salt[43]) to fit the spectrum.

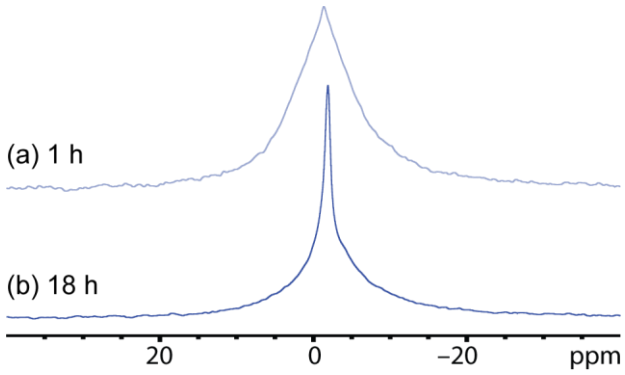

Figure 6. ^{7}Li ssNMR of c-AcH treated Cu soaked in LP30 for (a) 1 hour and (b) 18 hours. The spectra were acquired with a MAS frequency of 25 kHz.

After current has been passed, the electrolyte reduction products precipitate on the pre-existing N-SEI, resulting in the formation of the e-SEI. The ^{7}Li NMR spectra for N-SEI is compared to

those of the e-SEI pre-formed at 2 V, 1.4 V and 0.1 V voltage holds followed by Li plating of 0.5 mAh cm^{-2} at 1.2 mA cm^{-2} in Figure S8. For the e-SEI samples, the ^{7}Li resonances broaden with more negative applied voltage. The ^{7}Li spectra of e-SEI on Cu were fitted with 2-3 components, mainly LiF (~ -1 ppm) and Li_2CO_3 (~ 0 ppm) (Figure S9).[40] Additional components with positive ^{7}Li shifts (~ 0.6, ~ 1.6, ~3 ppm) were assigned to LiOH, Li_2O_2 and Li_2O (Figure S9). [40,43] The broadening of the ^{7}Li resonance and the appearance of the additional compounds indicates an increase in the diversity of the Li compounds in the e-SEI.[42]

***In situ* NMR** Measurements were performed on Cu –LFP cells for both surface treatments, d-HCl-Cu and c-AcH-Cu. In the beginning of each experiment the ^{7}Li signals observed (Figure S23a) are the signals from diamagnetic species (i.e., the electrolyte and the SEI) and the broad signal of the LFP. Due to the limited excitation bandwidth of the rf pulses, the broad signal for LFP is not fully excited and the use of ultra-wideline NMR experiments would be required to powder pattern; [30, 44] However, since only the Li metal signals are of interest, acquisition of the LFP powder pattern is not necessary. From the start of the plating a new signal emerges corresponding to the Li metal deposits. While the diamagnetic lithium resonances are close to 0 ppm, the Li metal resonance is easily distinguishable and shifted to approximately 260 ppm as a result of the Knight shift (Figure S23b).[45,46] Figure 7b shows the Li metal signal during electrodeposition on d-HCl-Cu, which grows in intensity during the electrodeposition and upon reversing the current, the signal decreases again. The electrochemistry is shown in Figure 7a (and in Figure S22), where the current density for the first cycle was 0.1 $mAcm^{-2}$ followed by four cycles using current density of 0.5 $mAcm^{-2}$. The amount of Li deposited was 1 $mAhcm^{-2}$, which results in an approximately 10μm thick Li metal layer on the Cu (assuming 100% efficiency and 50% coverage). The skin depth of the Li metal in this study is 12 μm so we expect to be fully exciting the deposited Li, which thus allows for quantification.

Integrating the ^{7}Li spectrum over the region of 220-300 ppm gives the total intensity of the Li metal signal detected by the NMR measurement upon plating and stripping on d-HCl-Cu and c-AcH-Cu (Figures 7c and 7d). The intensity is normalised to the total intensity at the end of charge for the first cycle. Comparing the two surface chemistries, the intensity of the Li metal resonance on the d-HCl-Cu grows with each cycle whereas that on the c-AcH-Cu it stays close to constant, with minimal increase between cycles. There are two possible explanations for an increase in the normalised Li metal intensity between cycles: i) the formation of so-called ‘dead Li’ as a result of inhomogeneous stripping increase the amount of Li metal in the cell between cycles. ii) A significant amount of the charge passed in the first cycles is used to form the SEI

or consumed in other parasitic reactions so that in the subsequent cycles the total amount of Li metal in the cell increases. As can be seen in Figure 7c,d, the amount of Li metal at the end of discharge is similar for both cells and increases around 3-7% at the first 5 cycles, which we attribute to dead-Li formation. However, the increase in Li metal for the d-HCl-Cu at the end of charge, corresponding to 1 mAhcm^{-2} capacity, is higher at about 20% for the second cycle and around 5-10% increase for the following cycles. Thus, we attribute the increase in Li metal intensity at the end of charge, not only to the accumulation of dead Li but as well to low current efficiency for Li metal plating in the first cycle, where part of the current is used for side reactions.

Interestingly, the Coulombic efficiency is almost identical for the two treatments (Figure S24), around 92-95%. Since galvanostatic cycling cannot distinguish between reversible faradaic reactions, the charge transferred due to any reversible reaction will add up to the measured capacity. This suggests that some of the side reactions on d-HCl-Cu are reversible, contrary to the SEI formation that is thought to be mostly irreversible. [6] In cycles 2-5 the amount of the cycled lithium metal increase since the extent of the parasitic reactions decreases.

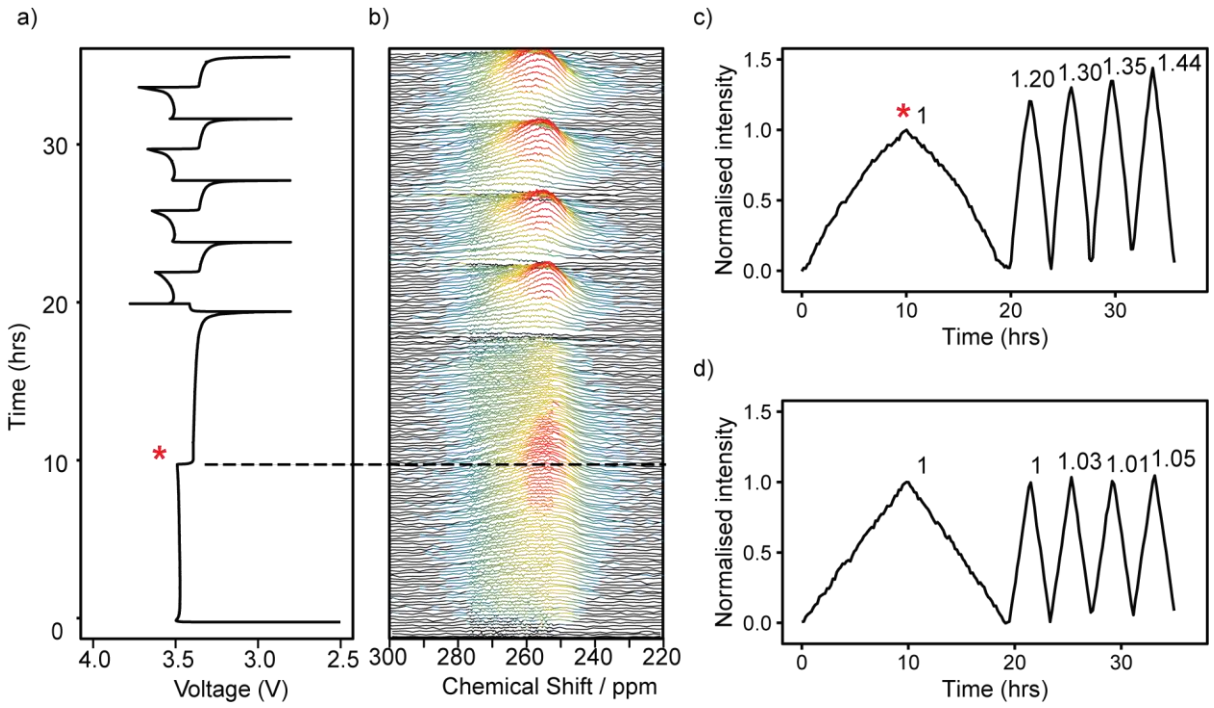

Figure 7. **a)** Galvanostatic cycling of *in* situ Cu-LFP cells using d-HCl-Cu where 0.01 mAcm^{-2} was used for the first cycle and 0.5 mAcm^{-2} for the subsequent cycles, plating and stripping 1 mAh cm^{-2} Li. **b)** *In situ* ^{7}Li NMR spectra obtained under the galvanostatic cycling of d-HCl-Cu. The normalised intensity detected by NMR of the Li metal peak, integrated over 220-300 ppm for **c)** d-HCl-Cu and **d)** c-AcH-Cu.

SEM: The effect of the Cu pretreatment on the resulting Li metal morphology was studied by SEM (Figure 8, top). Li was plated on Cu after a short rest time (<1 hour) at both low and high current densities (0.03 and 1.2 $mAcm^{-2}$, Figure 8, top and middle). Lower plating current gave rise to a smoother and denser Li morphology (Figure 8, top). Moreover, the Li plates on c-AcH-Cu more homogenously compared to d-HCl-Cu (Figures 8a and 8b). Furthermore, the Li is plated inside the channels on c-AcH-Cu (Figure 8a, top). When the N-SEI formation time prior to the plating is extended to twelve hours and plating at 1.2 $mAcm^{-2}$, results in thicker Li deposits (Figure 8, bottom).

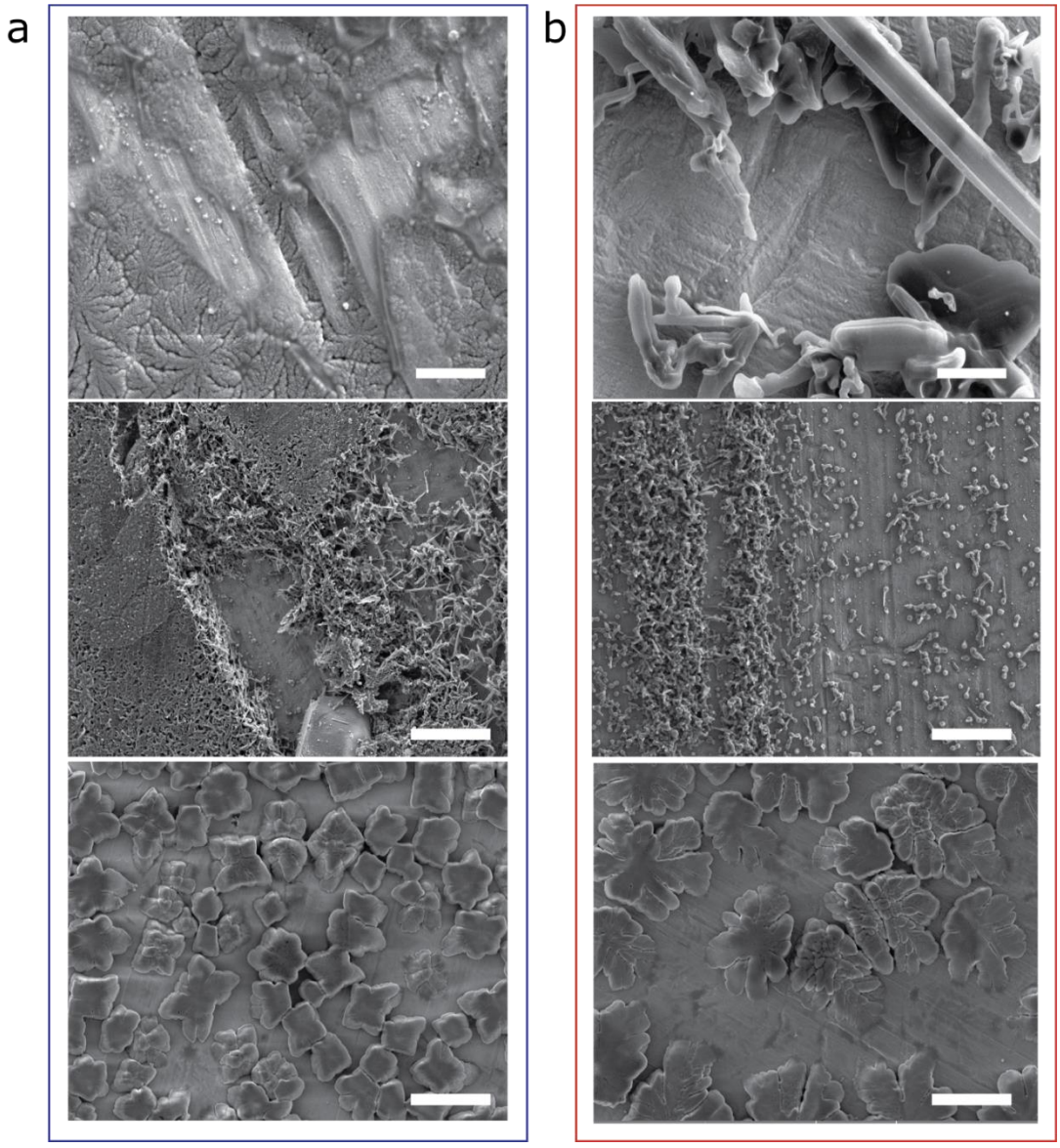

Figure 8. SEM of plated lithium microstructure. SEM images of lithium microstructures deposited on a) c-AcH-Cu and b) d-HCl-Cu disks using either a current density of 0.03 mA cm^{-2} (top) 1.2 mA cm^{-2} (middle and bottom), after either 1 hour rest (top and middle) or 12 hour rest (bottom). The scale bars are 2 μm in the top two images, 10 μm in the middle and bottom two.

The plating of Li results in inhomogeneous microstructures, typical in carbonate electrolytes (Figure 8), this could indicate a preferential plating of Li. To understand which compounds encourage Li plating, spatial distribution of the SEI was investigated using XPS and ToF-SIMS, both on Li plated and exposed Cu areas. When the SEI compounds correlate with Li coverage, the preferential Li plating can be attributed to the local composition of the SEI.

XPS on Li plated Cu: The XPS measurements show how both the SEI on exposed Cu surface and the plated lithium consists of similar carbon composites, with similar C1s spectra (Figures 9a and 9c). The C1s spectrum is dominated by C-C/C-H and -C-O and -O-C=O species on the surface, while on 10 nm sputtering additional peaks appear at 289.3 eV and 282.2 eV mainly due to the presence of Li_2CO_3 and Li_2C_2 respectively. [17]

The O 1s spectra of the exposed Cu surface changes significantly upon ~10 nm sputtering, revealing a new peak at 528 eV (Figure 9b), attributed to Li_2O.[36,47] The Li_2O peak at 528 eV was also observed on the O 1s spectrum of lithium plated areas, both on the surface and after ~10 nm sputtering (Figures 9b and 9d). The presence of Li_2O was further confirmed by the Li 1s peak at 53-54 eV (Figure S21).

The O 1s spectrum of SEI on the exposed Cu area (Figure 9b) consists of two broad peaks at 531.5 eV and 532.5 eV, assigned to OH^- and Li_2CO_3 at the surface. After the sputtering of 10 nm the OH^- peaks dominates around 531.0 eV.[36,48–51] The increased intensity of OH^- was observed on the exposed Cu surface by ToF-SIMS. [6,36]

The O 1s peak at 531.2 eV, was observed exclusively on the Li plated areas, which corresponds either to LiOH or to Li_2O_2 (Figure 9d). Since both O 1s and Li 1s characteristic binding energies for Li_2O_2 and LiOH are very close, the signals of those compounds cannot be separated. [36,47] However, since Li_2O_2 is known to be more stable in the XPS beam[36] and since this signal persisted during the sputtering (Figure 9d), this peak was assigned it to Li_2O_2.

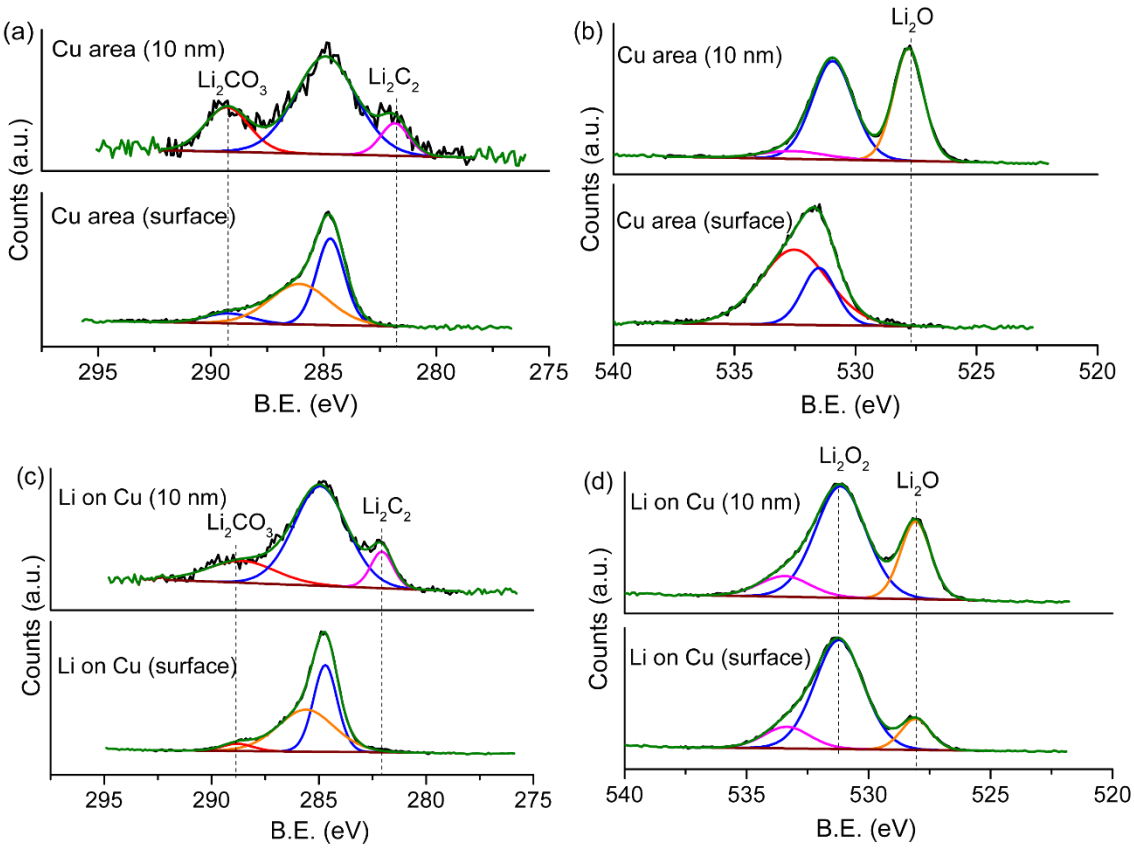

Figure 9. XPS of SEI on Cu exposed (a) C 1s (b) O 1s and Li plated Cu (c) C 1s (d) O 1s

TOF-SIMS: Li plating on Cu was studied with ToF-SIMS (Figure 10). CuO, LiF and OH^- (detected as ^{65}CuO, LiF_2^- and OH^-, respectively) were mapped on a 250 × 250 μm^2 area of Li plated samples (Figures 10, S28-33). The mapping was done on an area on the sample which visibly contained both areas of plated Li and exposed Cu surface. When the intensity of the studied SEI compound is in corroboration with Li coverage, the preferential Li plating can be attributed to the local composition of the SEI.

The CuO maps on the acquired area of the SEI on Li-plated and exposed Cu are depicted in Figures 10a and 10b. Interestingly, significant CuO signal was observed on the lithium plating areas, which indicates that Cu_xO is present in the SEI on the Li metal. Furthermore, the intensity of the Cu oxides on the Li metal is noticeably higher on the Li plated on d-HCl-Cu. A possible cause for this phenomenon could be more homogenous N-SEI formation on c-AcH-Cu, resulted in buried Cu oxides (see SI for 3D reconstruction at the XZ plane, Figure S28).

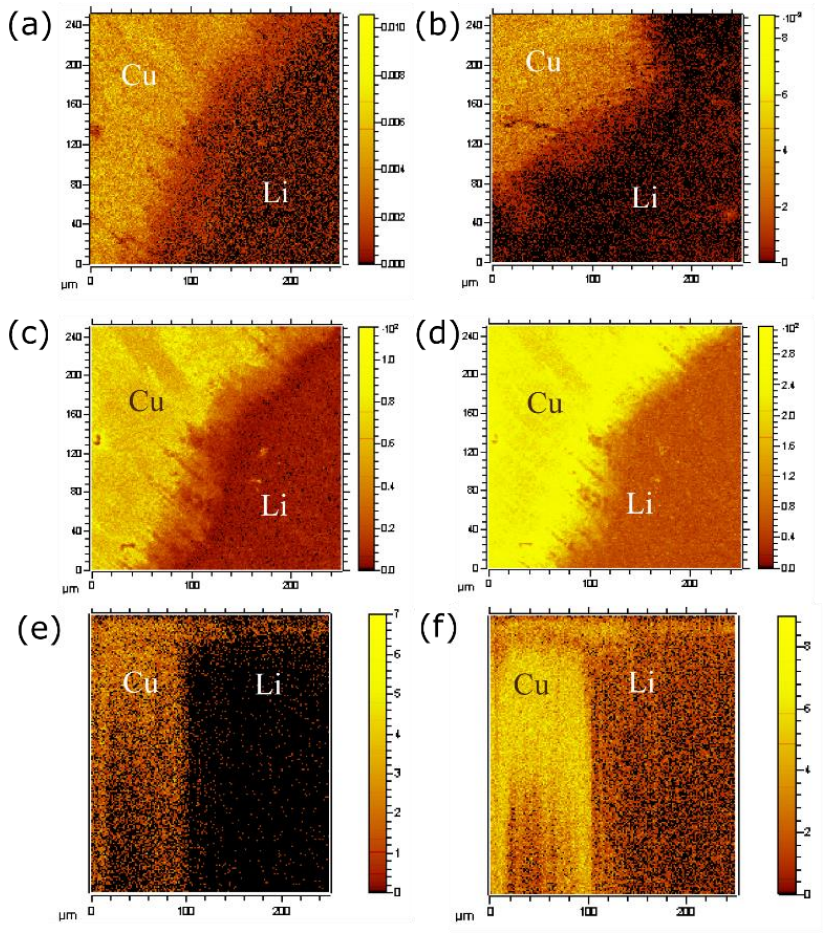

Figure 10. CuO ($^{65}CuO^-$) map of SEI on Li plated Cu for **(a)** d-HCl-Cu and **(b)** c-AcH-Cu. Maps of **(c)** LiF_2^-, **(d)** OH^- and **(e)** 3D reconstruction (XZ plane) of LiF_2^-, **(e)** OH^- of $eSEI_{0.1V}$ on Li plated d-HCl-Cu. Images a-d are point-to-point normalized to total counts. SEI on plated lithium and exposed copper areas is labelled as Li and Cu, accordingly.

The hydroxide group (OH^-) was found to give rise to high contrast maps and vastly different depth profiles when comparing plated and non-plated areas (Figures 10d,10f, S29a, S30-31). The OH^- map of $e\text{-}SEI_{0.1V}$ on Li plated d-HCl-Cu sample (Figure 10d) is depicted alongside its 3D reconstruction (XZ plane) (Figure 10f). A significantly higher intensity of the OH^- signal was observed for the SEI on the exposed Cu areas. Similar maps were shown for $e\text{-}SEI_{2V/0.1V}$ on c-AcH-Cu and d-HCl-Cu samples (Figures S29a, S30-31). The top surface of both areas is covered by a thin layer of OH^- (Figures 10f, S30b-31b). This layer is attributed to OH^- in the electrolyte decomposition products, which precipitated after the Li plating. Underneath the top layer there is a decrease in the intensity of the signal, presumably due to precipitation of SEI compounds other than OH^-. Deeper layers of the YX plane reveal a significantly higher intensity of the OH^- signal on the non-plated surface for both d-HCl-Cu and c-AcH-Cu samples. These findings support the assumption that the OH^- layer forms prior to Li plating and dictates the preferential areas for plating (Figures 10d, 10f, S30, S31).

The map of LiF (detected as $Li_2F_3^-$ or LiF_2^-) signal in the e-$SEI_{0.1V}$ on d-HCl-Cu (Figures 10c and 10) shows that similar to the OH- signal, the intensity of the LiF signal is consistently higher in areas with no plated Li. This indicates that there is preferential plating of Li in areas where the concentrations of LiF and OH^- are lower. A similar trend was observed for the LiF map of c-AcH-Cu samples (Figures S29b, S32b and S33b).

Discussion

The spontaneous formation of the N-SEI on the surface of Cu and Cu oxides, regardless of the surface treatment, was confirmed by ^{19}F and ^{7}Li ssNMR, EIS, XPS and ToF-SIMS. The N-SEI was shown to be mainly composed of LiF and $LiPF_6$ decomposition products in addition to copper oxides.

LiF was observed in the N-SEI with NMR, XPS and ToF-SIMS. Its formation on Cu at the OCV is assigned to the chemical decomposition of $LiPF_6$ due to its reaction with trace amounts of water (reactions 2-3).[41,52–55]

(2) $LiPF_6 \rightarrow LiF + PF_5$

(3) $PF_5 + H_2O \rightarrow PF_3O + 2HF$

Analysis of the ssNMR spectra revealed the existence of free fluoride ions in proximity to the Cu surface, resulting in ^{19}F NMR resonances at around -142 ppm and -225 ppm. While the resonance at -225 ppm is solely seen for the N-SEI, the resonance at -142 ppm is observed for both N-SEI and e-SEI_{2V} (Figures 5, S3-5).

Recently, Lebens-Higgins et al. assigned the ^{19}F NMR resonances around -144 ppm to F^- ions bounded to the surface of transition metal cathodes. Clément et al. [56] also reported a similar ^{19}F shift at -144 ppm, which was ascribed to lithiated fluoride on the electrode surface. [57] Here we assign both resonances (-144 ppm and -225 ppm) to free fluoride ions in various environments and proximities to the Cu oxide surface. Different chemical environments of the fluoride could be a result of the formation of various combinations of ion pairs and triplets, solvation of the fluoride ion and hydrogen bonds to OH^- group on Cu surface. [58,59]

Alternatively, the -225-ppm resonance on N-SEI could be assigned to the adsorbed fluoride ion monolayer. The latter is supported by the observation of $^{65}CuF_2$ SIMS signal on N-SEI and its decrease on e-SEI formed at constant potential under 2 V (Figure S27d). Since no CuF_2 resonances were observed in ^{19}F NMR of both N-SEI and e-SEIs, the above measurements were attributed solely to adsorbed fluoride ions, giving rise to various F^- resonances. These findings further support the assignment of the CV peaks in the range of 2.5-3.1 V to the

reduction of CuF_2 on the Cu surface (reaction 1).[16,35] The variation in the OCV of the Li-Cu half-cells is attributed to the interplay between the surface bonded Cu_xO, CuF_2 and the N-SEI.

The ^{19}F NMR resonance at -142 ppm was not observed for e-SEI formed at either 1.4 V or 0.1 V. Presumably, since these e-SEIs are thicker than e-SEI_{2V} and e-$SEI_{0.1V}$, the mobility of the formed fluoride ions is reduced and most of it is not in proximity to the Cu surface, resulting in the general resonance for LiF at -204 ppm.

A narrowing of the ^{7}Li resonances was observed for longer N-SEI formation times and broadening with decreasing e-SEI formation voltages (Figure S8). The narrowing is tentatively ascribed to the formation of mobile free Li ions in proximity to the Cu. After the passage of current an increase of compound diversity and formation of the majority of LiF in the SEI bulk (less mobile) leads to a broadening of the signal (Figure S8). [42]

The XPS analysis of the N-SEI indicates that it is composed of Cu oxides, LiF, $LiPF_6$ decomposition products (Li_xPF_y, $Li_xPO_yF_z$), while the e-SEI formed at 2 V and 1.4 V contains additional PEO-like compounds (Figures S16-19). The sequential reactions (4)-(5) represent a possible reaction mechanism for OH^- formation. [28,37,60,61] The PEO-like oligomers are formed via OH^- driven EC hydrolysis.[62] Reactions i-iii represent the reaction mechanism for reaction 4, suggested by Martin et al.[9,10,20,21,25,36,52]

(4) $CuO + 2Li \leftrightarrow Li_2O + Cu$

i. $CuO + 1/2Li \leftrightarrow 1/2Cu_2O + 1/4Li_2O_2$

ii. $1/2Cu_2O + 1/4Li_2O_2 + Li \leftrightarrow Cu + 1/4Li_2O_2 + 1/2Li_2O$

iii. $Cu + 1/4Li_2O_2 + 1/2Li_2O + 1/2Li \leftrightarrow Cu + Li_2O$

(5) $Li_2O + HF \rightarrow LiF + OH^- + Li^+$

Comparing the LiF:$LiPF_6$ ratio in the F 1s spectra, it seems that LiF is the main species in both the N-SEI and e-SEI_{2V}, while for the e-$SEI_{1.4V}$, $LiPF_6$ species (Li_xPF_y, $Li_xPO_yF_z$) signal is more dominant on the surface, with the LiF signal only observed after sputtering (Figures S16-17, Table S2). This could be the result of the formation of LiF both chemically and electrochemically mainly during rest or at the first stages of SEI formation. This assumption is further supported with the LiF ToF-SIMS depth profile, in which the intensity of the LiF signal is significantly higher for e-SEI formed at either 2.8 V or 2 V (Figure S27a). The formation of a thick SEI, mainly composed of LiF, on lithiated CuO is masking both the Cu 2p and O 1s signals of Cu oxides (Figure S15). Martin et al. [28] observed, using XPS, selective formation of

LiF on CuO surface at reduction potentials above 1.4 V. This suggests that LiF is a product of the Cu oxide reduction at 2-1.3 V (reactions 4-5).

A Li_2O signal, observed in both Li plated and exposed Cu areas, is an indication for reduction of Cu oxide prior to or during Li plating (Figures 9b and 9d). [25,36] A negative shift of the Cu 2p peaks was assigned to the lithiation of the Cu oxides (Figure S15, S20), which could be a possible reason for an additional thickening of the SEI at 1.4 V. [23] However, Li_2O was not observed in neither of the acquired ^{7}Li NMR spectra of SEI on Cu. Presumably, this is due to the low concentration of Li_2O in the SEI relatively to other $LiPF_6$ decomposition products.

Li_2O_2 was observed mainly on the Li plated areas (Figure 9d). The increased concentration of Li_2O_2 may encourage the formation of highly conducting grain boundaries and, as a result, preferential plating of Li. [59,63–65] The mechanism of Li_2O_2 formation on a Cu surface is explained by equation 3 and occurs at potentials lower than 2.14 V. LiOH was observed in the O 1s XPS spectrum (Figures 9b) on the exposed Cu areas. [36,47–49] These findings support the preferential plating on OH^--deficient and Li_2O_2 rich SEI.

Li carbide (Li_2C_2) was found by XPS (Figures 9a and 9c) in the inner layer of the SEI. Li_2C_2 was observed previously on Li plated Cu. [4] However, on the contrary to the observations of Eshetu et al. [17], for the samples tested herein, it was observed on both the plated-Li and exposed Cu areas. Li_2C_2 was observed on Li-plated samples by ToF-SIMS as well; however due to the presence of several substances with similar masses in the SEI, the signal of Li_2C_2 cannot be normalized to the total ion concentration. These findings agree with the findings of Schmitz et al. [4] and it is likely formed by the reduction of Li_2CO_3[66] or organic SEI components. Further study is required in order to understand the role of non-stoichiometric Li_2C_2 formation during Li plating.

CuO was found using ToF-SIMS in the SEI on both Li plated and exposed Cu areas (Figure 10). The intensity of Cu oxides on the surface of Li plated on d-HCl-Cu is noticeably higher. These findings suggest that Cu oxides migrate from the N-SEI to the SEI. However, since the intensity of CuO is similar on the Li plated and exposed Cu areas, Cu oxides do not seem to be the cause for preferential plating.

The coulombic efficiency of lithium plating and striping was the same for both Cu treatments, however the trend of Li metal observed with *in-situ* NMR was very different (Figure S24). We attribute this phenomenon to semi-reversible electrochemical reactions, which occur together

with the Li plating and stripping on d-HCl-Cu. Moreover, the typical reduction and oxidation waves for those processes in the literature are roughly matching the ones observed in the cyclic voltammetry of the Cu-Li cells for both Cu treatments (Figures 3 and S25).[67] The contribution of these reactions to the electrochemical efficiency diminishes in the first five cycles, thus the amount of the cycled lithium metal increase.

Since most SEI reactions are not reversible, the observed trends can be assigned to either the lithiation on CuO or to the reversible lithiation of basic $CuCO_3$ (reactions 6-7). [68] As the Cu oxide layer is typically not thicker than 10 nm[25], it cannot contribute more than ~10 µAh/cm^2 to the overall capacity (about 4% of the observed parasitic capacity). Thus we attribute this effect to a combination of Cu oxide reversible reduction and to the reversible electrochemical reaction of basic carbonates (reactions 8-10).[69]

(6) $Cu(OH)_2 + 2Li^+ + 2e^- \rightarrow Cu + 2LiOH$

(7) $Li_2CO_3 + Cu \leftrightarrow CuCO_3 + 2Li^+ + 2e^-$

ToF-SIMS study of the SEI composition revealed preferential Li plating on OH^- and LiF deficient areas, which is in corroboration with XPS findings. The signals of OH^- and LiF are consistently higher from the SEI on non-plated Cu compared to the ones from the SEI on Li metal for both Cu treatments.

The OH^- and LiF signals from N-SEI on c-AcH-Cu are lower and more homogeneous (Figures 10, S29-S33). We attribute the smoother Li morphology on c-AcH-Cu to more homogeneous distribution of OH^- and LiF on N-SEI. A possible explanation to this effect could be the depression of LiF conductivity by the presence of OH^-. [59,70] The ionic conductivity decrease is caused by the formation of hydrogen bonds between the fluoride in LiF and the hydrogen on OH^-, limiting the mobility of Li ions. However, since in the system studied herein, both Cu and Li can interact with the OH^-, further study is required to fully explain these findings.

Conclusions

A native, inorganic SEI-like layer, composed of LiF, $LiPF_6$ decomposition products, Cu oxides and fluorides spontaneously form on Cu current collectors upon their immersion in $LiPF_6$-based electrolytes. LiF in the N-SEI is formed by multi-step reaction of $LiPF_6$ with trace amounts of water and it exists both in solid form and as free Li^+ and F^- ions. The passivating properties of the N-SEI are influenced by the Cu oxide layer homogeneity and chemical

composition. The OCV of the cells is determined by the copper interface composition, homogeneity and formation time. The electrochemically formed SEI on Cu is composed of N-SEI as the primary layer, Cu oxide reduction and lithiation products (Li_xCuO, Li_2O, Li_2O_2 and OH^-) and solvent reduction products.

In situ NMR was used to measure the Li plating efficiency, revealing semi-reversible electrochemical reactions during the first cycle, assigned to the reversible reduction of copper species in the SEI.

The preferential plating seen with both XPS and ToF-SIMS is governed by the distribution of low ionic conducting compounds (LiF, OH^-, Li_2O_2, Li_2O) rather than electronic conducting compounds (Cu, CuO, Li_2C_2). Thus, we suggest that the cause for preferential plating is the significant variance in the ionic conductivity of SEI components giving rise to heterogeneous current density distribution on the Cu surface and results in heterogeneous Li coverage and morphology.

Li plating on Cu is affected by the interplay between the SEI components and SEI homogeneity. A homogeneous SEI composition, will give rise to a homogeneous current density and smother Li morphology. Since a OH^--rich Cu surface encourages SEI homogeneity, it is preferred, in spite of its higher impedance.

Acknowledgements:

SM acknowledge the funding from the Blavatnik Cambridge Fellowships. A.B.G acknowledges the support from the Royal Society (RP/R1/180147) and EPSRC-EP/M009521/1 for funding. The X-ray photoelectron (XPS) data collection was performed at the EPSRC National Facility for XPS ("HarwellXPS"), operated by Cardiff University and UCL, under Contract No. PR16195.Via our membership of the UK's HEC Materials Chemistry Consortium, which is funded by EPSRC (EP/L000202),

References

1. Liu, J. *et al.* Pathways for practical high-energy long-cycling lithium metal batteries.

Nat. Energy **4**, 180–186 (2019).

2. Qian, J. *et al.* Anode-Free Rechargeable Lithium Metal Batteries. *Adv. Funct. Mater.* **26**, 7094–7102 (2016).

3. Neudecker, B. J., Dudney, N. J. & Bates, J. B. 'Lithium-free' thin-film battery with in situ plated Li anode. *J. Electrochem. Soc.* **147**, 517–523 (2000).

4. Schmitz, R. *et al.* SEI investigations on copper electrodes after lithium plating with Raman spectroscopy and mass spectrometry. *J. Power Sources* **233**, 110–114 (2013).

5. Menkin, S., Golodnitsky, D. & Peled, E. Artificial solid-electrolyte interphase (SEI) for improved cycleability and safety of lithium-ion cells for EV applications. *Electrochem. commun.* **11**, (2009).

6. Peled, E. & Menkin, S. Review — SEI : Past , Present and Future. *J. Electrochem. Soc.* **164**, (2017).

7. Li, Q. *et al.* Homogeneous Interface Conductivity for Lithium Dendrite-Free Anode. *ACS Energy Lett.* **3**, 2259–2266 (2018).

8. Hao, F., Verma, A. & Mukherjee, P. P. Mechanistic insight into dendrite-SEI interactions for lithium metal electrodes. *J. Mater. Chem. A* **6**, 19664–19671 (2018).

9. Myung, S. T., Sasaki, Y., Sakurada, S., Sun, Y. K. & Yashiro, H. Electrochemical behavior of current collectors for lithium batteries in non-aqueous alkyl carbonate solution and surface analysis by ToF-SIMS. *Electrochim. Acta* **55**, 288–297 (2009).

10. Kitz, P. G., Lacey, M. J., Novák, P. & Berg, E. J. Operando EQCM-D with Simultaneous in Situ EIS: New Insights into Interphase Formation in Li Ion Batteries. *Anal. Chem.* **91**, 2296–2303 (2019).

11. Lin, D. *et al.* Fast galvanic lithium corrosion involving a Kirkendall-type mechanism. *Nat. Chem.* **11**, 382–389 (2019).

12. Huang, W. *et al.* Nanostructural and Electrochemical Evolution of the Solid-Electrolyte Interphase on CuO Nanowires Revealed by Cryogenic-Electron Microscopy and Impedance Spectroscopy. *ACS Nano* **13**, 737–744 (2019).

13. Guidotti, R. A. & Nelson, G. C. PASSIVE-FILM FORMATION ON METAL

SUBSTRATES IN IM LiPF/EC-DMC SOLUTIONS RONALD. *Mat. Res. Soc. Symp. Proc.* **496**, 469–475 (1998).

14. Andersson, A. M., Henningson, A., Siegbahn, H., Jansson, U. & Edström, K. Electrochemically lithiated graphite characterised by photoelectron spectroscopy. *J. Power Sources* **119**–**121**, 522–527 (2003).

15. Goh, S. W., Buckley, A. N., Skinner, W. M. & Fan, L.-J. An X-ray photoelectron and absorption spectroscopic investigation of the electronic structure of cubanite, CuFe2S3. *Phys. Chem. Miner.* **37**, 389–405 (2010).

16. Fiedler, C., Luerssen, B., Rohnke, M., Sann, J. & Janek, J. XPS and SIMS analysis of solid electrolyte interphases on lithium formed by ether-based electrolytes. *J. Electrochem. Soc.* **164**, A3742–A3749 (2017).

17. Eshetu, G. G. *et al.* In-Depth Interfacial Chemistry and Reactivity Focused Investigation of Lithium-Imide- and Lithium-Imidazole-Based Electrolytes. *ACS Appl. Mater. Interfaces* **8**, 16087–16100 (2016).

18. Jung, E. Y. *et al.* Experimental study on solid electrolyte interphase of graphite electrode in Li-ion battery by surface analysis technique. *Mol. Cryst. Liq. Cryst.* **663**, 158–167 (2018).

19. Hua, X. *et al.* Comprehensive study of the CuF2 conversion reaction mechanism in a lithium ion battery. *J. Phys. Chem. C* **118**, 15169–15184 (2014).

20. Novák, P. CuO cathode in lithium cells-III. Its discharge kinetics. *Electrochim. Acta* **31**, 1167–1173 (1986).

21. Novák, P. CuO cathode in lithium cells-II. Reduction mechanism of CuO. *Electrochim. Acta* **30**, 1687–1692 (1985).

22. Benedeti, A. V., Sumodjo, P. T. A., Nobe, K., Cabot, P. L. & Proud, W. G. Electrochemical studies of copper, copper-aluminium and copper-aluminium-silver alloys: Impedance results in 0.5M NaCl. *Electrochim. Acta* **40**, 2657–2668 (1995).

23. Chen, W., Zhang, H., Ma, Z., Yang, B. & Li, Z. High electrochemical performance and lithiation-delithiation phase evolution in CuO thin films for Li-ion storage. *J. Mater. Chem. A* **3**, 14202–14209 (2015).

24. Malitesta, C., Rotunno, T., Sabbatini, L. & Zambonin, P. G. Insight into the intercalation problem of the Li/CuO cell by analytical electron spectroscopies. *J. Chem. Soc. Faraday Trans.* **86**, 3607–3611 (1990).

25. Yamakawa, N., Jiang, M. & Grey, C. P. Investigation of the conversion reaction mechanisms for binarycopper(ii) compounds by solid-state nmr spectroscopy and X-ray diffraction. *Chem. Mater.* **21**, 3162–3176 (2009).

26. An, S. J. *et al.* The state of understanding of the lithium-ion-battery graphite solid electrolyte interphase (SEI) and its relationship to formation cycling. *Carbon N. Y.* **105**, 52–76 (2016).

27. Assegie, A. A., Cheng, J. H., Kuo, L. M., Su, W. N. & Hwang, B. J. Polyethylene oxide film coating enhances lithium cycling efficiency of an anode-free lithium-metal battery. *Nanoscale* **10**, 6125–6138 (2018).

28. Martin, L., Martinez, H., Poinot, D., Pecquenard, B. & Le Cras, F. Direct observation of important morphology and composition changes at the surface of the CuO conversion material in lithium batteries. *J. Power Sources* **248**, 861–873 (2014).

29. Chavez, K. L. & Hess, D. W. A Novel Method of Etching Copper Oxide Using Acetic Acid. *J. Electrochem. Soc.* **148**, 640–643 (2001).

30. Pecher, O., Carretero-Gonzalez, J., Griffith, K. J. & Grey, C. P. Materials' methods: NMR in battery research. *Chem. Mater.* **29**, 213–242 (2017).

31. Ross Macdonald, E. B. *Fundamentals of Impedance Spectroscopy*.

32. Diard, Jean-Paul & Le Gorrec, Bernard & Montella, C. *Handbook of Electrochemical Impedance Spectroscopy CIRCUITS made of RESISTORS and CAPACITORS.* (2007). doi:10.13140/RG.2.2.25393.12641.

33. IRVINE, J. T. S., SINCLAIR, D. C. & WEST, A. R. ChemInform Abstract: Electroceramics: Characterization by Impedance Spectroscopy. *ChemInform* **21**, 132–138 (2016).

34. Balbuena, P. B. *Lithium-Ion Batteries Solid-Electrolyte Interphase*. (Imperial College Press, 2004).

35. Omenya, F. *et al.* Intrinsic Challenges to the Electrochemical Reversibility of the High Energy Density Copper(II) Fluoride Cathode Material. *ACS Appl. Energy Mater.* **2**, 5243–5253 (2019).

36. Martin, L., Martinez, H., Poinot, D., Pecquenard, B. & Le Cras, F. Comprehensive X-ray photoelectron spectroscopy study of the conversion reaction mechanism of CuO in lithiated thin film electrodes. *J. Phys. Chem. C* **117**, 4421–4430 (2013).

37. Biesinger, M. C. Advanced analysis of copper X-ray photoelectron spectra. *Surf. Interface Anal.* **49**, 1325–1334 (2017).

38. Campion, C. L., Li, W. & Lucht, B. L. Thermal decomposition of LiPF 6-based electrolytes for lithium-ion batteries. *J. Electrochem. Soc.* **152**, 2327–2334 (2005).

39. Wiemers-Meyer, S., Jeremias, S., Winter, M. & Nowak, S. Influence of Battery Cell Components and Water on the Thermal and Chemical Stability of LiPF6 Based Lithium Ion Battery Electrolytes. *Electrochim. Acta* **222**, 1267–1271 (2016).

40. Meyer, B. M., Leifer, N., Sakamoto, S., Greenbaum, S. G. & Grey, C. P. High Field Multinuclear NMR Investigation of the SEI Layer in Lithium Rechargeable Batteries. 145–148 (2005) doi:10.1149/1.1854117.

41. Plakhotnyk, A. V., Ernst, L. & Schmutzler, R. Hydrolysis in the system LiPF 6 - Propylene carbonate - Dimethyl carbonate - H 2O. *J. Fluor. Chem.* **126**, 27–31 (2005).

42. Breuer, S., Pregartner, V., Lunghammer, S. & Wilkening, H. M. R. Dispersed Solid Conductors: Fast Interfacial Li-Ion Dynamics in Nanostructured LiF and LiF γ-Al2O3 Composites. *J. Phys. Chem. C* **123**, 5222–5230 (2019).

43. Huff, L. A. *et al.* Identification of Li-Ion Battery SEI Compounds through 7Li and 13C Solid-State MAS NMR Spectroscopy and MALDI-TOF Mass Spectrometry. *ACS Appl. Mater. Interfaces* **8**, 371–380 (2016).

44. Schurko, R. W. Ultra-wideline solid-state NMR spectroscopy. *Acc. Chem. Res.* **46**, 1985–1995 (2013).

45. KNIGHT, W. D. Nuclear Magnetic Resonance Shift in Metals. *Phys. Rev.* **76**, 1259 (1949).

46. Trease, N. M., Zhou, L., Chang, H. J., Zhu, B. Y. & Grey, C. P. In situ NMR of lithium ion batteries: Bulk susceptibility effects and practical considerations. *Solid State Nucl. Magn. Reson.* **42**, 62–70 (2012).

47. Yao, K. P. C. *et al.* Thermal stability of Li2O2 and Li2O for li-air batteries: In situ XRD and XPS studies. *J. Electrochem. Soc.* **160**, 824–831 (2013).

48. Svintsitskiy, D. A., Slavinskaya, E. M., Kardash, T. Y., Avdeev, V. I. & Senkovskiy, B. V. Applied Catalysis A : General Low-temperature catalytic CO oxidation over mixed silver – copper. *Appl. Catal., A* **510**, 64–73 (2016).

49. Nücker, N., Fink, J., Fuggle, J. C., Durham, P. J. & Temmerman, W. M. Evidence for holes on oxygen sites in the high-Tc superconductors La2-xSrxCuO4 and YBa2Cu3O7-y. *Phys. Rev. B* **37**, 5158–5163 (1988).

50. Tanaka, S., Taniguchi, M. & Tanigawa, H. XPS and UPS studies on electronic structure of Li2O. *J. Nucl. Mater.* **283**–**287**, 1405–1408 (2000).

51. Zatsepin, D. A. *et al.* Valence states of copper ions and electronic structure of LiCu2O2. *Phys. Rev. B* **57**, 4377–4381 (1998).

52. Strmcnik, D. *et al.* Electrocatalytic transformation of HF impurity to H2 and LiF in lithium-ion batteries. *Nat. Catal.* **1**, 255–262 (2018).

53. Solchenbach, S., Metzger, M., Egawa, M., Beyer, H. & Gasteiger, H. A. Quantification of PF5 and POF3 from side reactions of LiPF6 in li-ion batteries. *J. Electrochem. Soc.* **165**, A3022–A3028 (2018).

54. Aurbach, D., Markovsky, B., Shechter, A., Ein-Eli, Y. & Cohen, H. A comparative study of synthetic graphite and Li electrodes in electrolyte solutions based on ethylene carbonate-Dimethyl carbonate mixtures. *J. Electrochem. Soc.* **143**, 3809–3820 (1996).

55. Rinkel, B., Hall, D. S., Temprano, I. & Grey, C. P. Electrolyte oxidation pathways in lithium-ion batteries. *J. Am. Chem. Soc.* (2020) doi:10.1021/jacs.0c06363.

56. Clément, R. J., Kitchaev, D., Lee, J. & Gerbrand Ceder. Short-Range Order and Unusual Modes of Nickel Redox in a Fluorine-Substituted Disordered Rocksalt Oxide Lithium-Ion Cathode. *Chem. Mater.* **30**, 6945–6956 (2018).

57. Co, L. *et al.* Surface Chemistry Dependence on Aluminum Doping in Ni-rich. 1–12 (2019) doi:10.1038/s41598-019-53932-6.

58. Scholz, G., Stosiek, C., Noack, J. & Kemnitz, E. Local fluorine environments in nanoscopic magnesium hydr(oxide) fluorides studied by 19F MAS NMR. *J. Fluor. Chem.* **132**, 1079–1085 (2011).

59. T.G.Stoebe. Influence of OH- ions on infrared absorption and ionic conductivity in lithium fluoride crystals. *J. Phys. Chnn. Solid Fergamon* **28**, 1375–1382 (1967).

60. Biesinger, M. C., Hart, B. R., Polack, R., Kobe, B. A. & Smart, R. S. C. Analysis of mineral surface chemistry in flotation separation using imaging XPS. *Miner. Eng.* **20**, 152–162 (2007).

61. Biesinger, M. C., Lau, L. W. M., Gerson, A. R. & Smart, R. S. C. Resolving surface chemical states in XPS analysis of first row transition metals, oxides and hydroxides: Sc, Ti, V, Cu and Zn. *Appl. Surf. Sci.* **257**, 887–898 (2010).

62. Metzger, M., Strehle, B., Solchenbach, S. & Gasteiger, H. A. Hydrolysis of Ethylene Carbonate with Water and Hydroxide under Battery Operating Conditions. *J. Electrochem. Soc.* **163**, A1219–A1225 (2016).

63. Tian, F., Radin, M. D. & Siegel, D. J. Enhanced charge transport in amorphous Li2O2. *Chem. Mater.* **26**, 2952–2959 (2014).

64. Gileadi, E. *Electrode Kinetics for and Materials Scientists*. *VCH* (1993).

65. Gerbig, O., Merkle, R. & Maier, J. Electron and ion transport in Li2O2. *Adv. Mater.* **25**, 3129–3133 (2013).

66. McShane, E. J. *et al.* Quantification of Inactive Lithium and Solid-Electrolyte Interphase Species on Graphite Electrodes after Fast Charging. *ACS Energy Lett.* **5**, 2045–2051 (2020).

67. Tian, N., Hua, C., Wang, Z. & Chen, L. Reversible reduction of Li2CO3. 14173–14177 (2015) doi:10.1039/c5ta02499d.

68. Shao, L. *et al.* Preparation and characterization of basic carbonates as novel anode materials for lithium-ion batteries. *Ceram. Int.* **40**, 3105–3116 (2014).

69. Leon, J. J. D. *et al.* Reflectometry − Ellipsometry Reveals Thickness, Growth Rate, and Phase Composition in Oxidation of Copper. *ACS Appl. Mater. Interfaces* (2016) doi:10.1021/acsami.6b06626.

70. Wang, E., Dey, S., Liu, T., Menkin, S. & Grey, C. P. Effects of Atmospheric Gases on Li Metal Cyclability and Solid-Electrolyte Interphase Formation. *ACS Energy Lett.* 1088–1094 (2020) doi:10.1021/acsenergylett.0c00257.

71. Irvine, B. J. T. S., Sinclair, D. C. & West, A. R. <Electroceramics Characterisation by impedance sepctroscopy.pdf>. **2**, 132–138 (1990).

72. Eshkenazy, V. THE ROLE OF SEI IN LITHIUM AND LITHIUM ION BATTERIES E. PELED, D. GOLODNITSKY, G. ARDEL, C. MENACHEM, D. BAR TOW AND V. ESHKENAZY School of Chemistry, Tel Aviv University, Tel Aviv 69978, Israel. **393**, 209–221 (2020).

73. Campion, C. L., Li, W. & Lucht, B. L. Thermal Decomposition of LiPF 6 -Based Electrolytes for Lithium-Ion Batteries. *J. Electrochem. Soc.* **152**, A2327–A2334 (2005).

74. Grey, C. P. & Corbin, D. R. 19F and 27Al MAS NMR study of the dehydrofluorination reaction of hydrofluorocarbon-134 over basic faujasite zeolites. *J. Phys. Chem.* **99**, 16821–16823 (1995).

75. Wiemers-Meyer, S., Winter, M. & Nowak, S. Mechanistic insights into lithium ion battery electrolyte degradation-a quantitative NMR study. *Phys. Chem. Chem. Phys.* **18**, 26595–26601 (2016).

76. Shenderovich, I. G. *et al.* Low-temperature NMR studies of the structure and dynamics of a novel series of acid-base complexes of HF with collidine exhibiting scalar couplings across hydrogen bonds. *J. Am. Chem. Soc.* **125**, 11710–11720 (2003).

77. Magnetic, N. & Studies, R. of Ion. 1878–1883 (1977).

78. Burkstrand, J. M. Unusual core level spectra of copper on polystyrene. *Surf. Sci.* **78**, 513–517 (1978).

79. Notes, S. & Kotzur, D. Influence of the Skin Effect on the Bloch Decay in Metals. *phys stat. sol.* **25**, (1972).

80. Ilott, A. J. & Jerschow, A. Super-resolution Surface Microscopy of Conductors using Magnetic Resonance. *Sci. Rep.* **7**, 1–7 (2017).

81. Kittel, C. Introduction to Solid State Physics, 8th edition. *Wiley Sons, New York, NY* (2004).

82. Lide, D. R. CRC Handbook of Chemistry and Physics, 84th Edition, 2003-2004. *Handb. Chem. Phys.* (2003) doi:10.1136/oem.53.7.504.

83. Gardam, G. E. The evaluation of throwing power in electrodeposition. *Trans. Faraday Soc.* **34**, 698–711 (1938).

Supplementary information

EIS study of N-SEI

To explore the N-SEI further, the impedance of Cu-Cu symmetric cells was measured as function of time . The EIS Nyquist plot of d-HCl-Cu symmetrical cells is typical for a linear restricted diffusion towards a blocking electrode (Figure 2a in the manuscript).

The plots of c-AcH-Cu symmetric cell were fitted with a Randomize + Simplex fitting method with 200,000 iterations for each step. The Nyquist plot measured after one hour rest time, was fitted with Voigt-type equivalent circuit a R1+Q1/(R2+Wd1)+Q4/R4 (Figure S1, Table S1). R1 was assigned to the impedance of the bulk electrolyte. R2, R4 and Q1, Q4 were assigned to the impedance and capacitance of different phases in the N-SEI. The confined finite length diffusion component (Wd), typically assigned to mass transport through a layer with a finite length, was assigned to the mass transfer in the N-SEI (Figure S1).

The semi-circles at frequencies above 100 kHz, are typically assigned to the compact surface films adjacent to a metal surface.[31,34,71] An equivalent circuit composed of multiple RC units was previously assigned to SEI.[34] The maximum of the high frequency semi-circle is at approximately 165 kHz and its capacitance is of the order of 10^{-9} F (Figures 2b and S1, Table S1). Alternatively, the relatively low capacitance of the semi-circle (around 10^{-9} F) also could be due to the significant roughness of the Cu substrate. [72]

After five days of rest, an additional R-Q component was needed to fit the impedance response, although the total impedance was not changed scientifically (Figure S2, Table S1). This could be an indication for an increase in the heterogeneity of the SEI after prolong rest time.

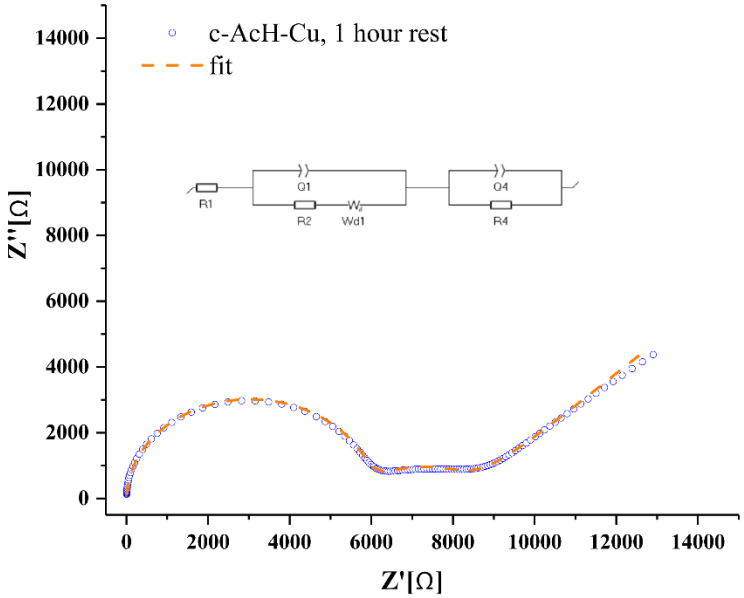

Figure S1. PEIS in the 1 MHz – 1 Hz frequency range, with an amplitude of 10 mV, Nyquist plot in symmetric cells of N-SEI on c-AcH-Cu after 1-hour rest (blue) and the equivalent circuit fit (orange, see circuit insert).

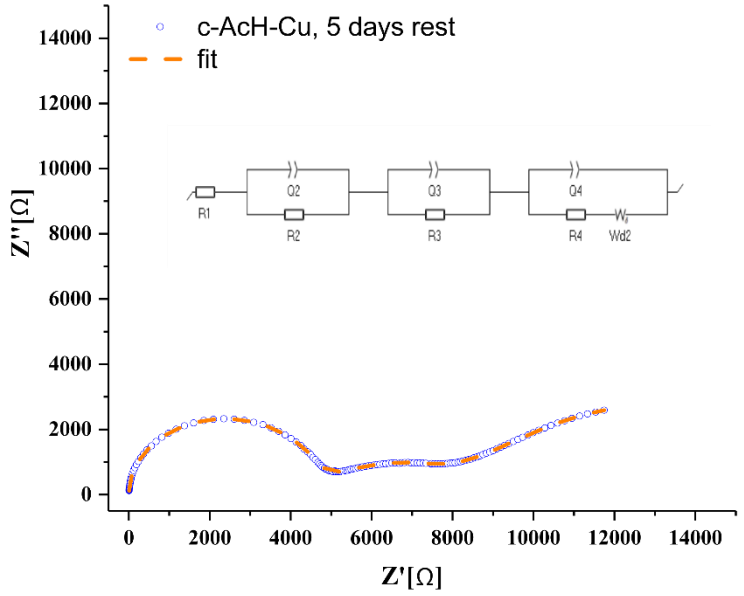

Figure S2. PEIS in the 1 MHz – 1 Hz frequency range, with an amplitude of 10 mV, Nyquist plot in symmetric cells of N-SEI on c-AcH-Cu after 5-day rest (blue) and the equivalent circuit fit (orange, see circuit insert).

Table S1. The resulting fitting parameters for the c-AcH-Cu symmetric cells shown in Figure S1 and Figure S2.

Parameter	Value for t_{rest}=1 hour	Value for t_{rest}=5 days
R2 [Ω]	2488	4571
R3 [Ω]	5897	955
R4 [Ω]	NA	3034
Q2, a2 [$Fs^{(a-1)}$]	0.4e-6, 0.75	0.2e-9, 1
Q3,a3 [$Fs^{(a-1)}$]	0.2e-9, 1	0.3e-6, 0.8
Q4,a4 [$Fs^{(a-1)}$]	NA	2.8e-6, 0.65
Rd2 [Ω] (Wd)	5897	5648
Fit $\chi/\lvert z \rvert$	0.04	0.03

^{19}F and 7Li SSNMR

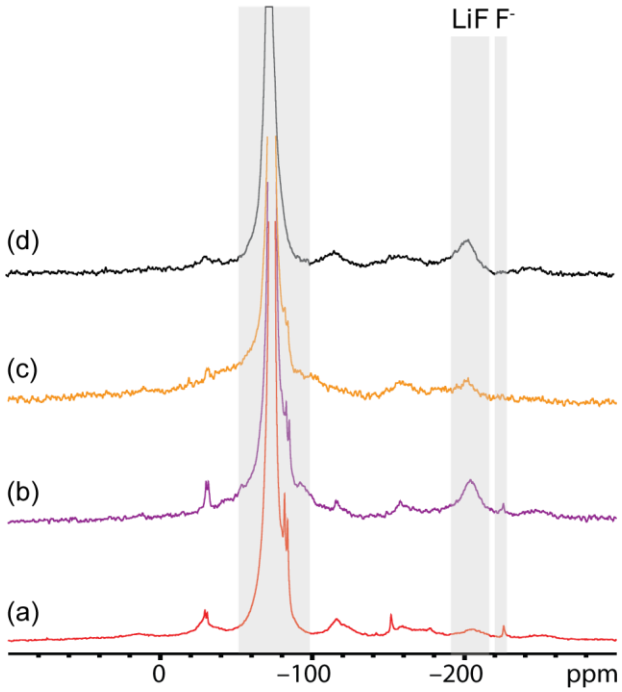

Figure S3. ^{19}F SSNMR spectra of the N-SEI on (a) d-HCl treated copper, (b) CuO, (c) Cu_2O and (d) lithium metal soaked in LP30 for over 30 hours.

The effect of soaking time was studied by comparing the ^{19}F NMR spectra of samples of d-HCl-Cu soaked for 1 hour and 96 hours and of c-AcH-Cu soaked for 1 hour and 18 hours (Figure S4). Both sets of spectra consist of resonances corresponding to $LiPF_6$ and its decomposition products and a broad LiF resonance.[73] In addition, sharp resonances around -225 ppm were observed in all spectra except c-AcH-Cu soaked for 1 hour.

In all the ^{19}F NMR spectra (Figures 5, S3-5, S8-9), a group of poorly resolved resonances in the range of -130 ppm to -180 ppm appears in varying intensities (detailed in Figure S5). The -156 ppm and -153 ppm resonances are attributed to HF in several publications.[57] However, it is not fully understood how HF can co-exist with lithium metal. The resonance around -180 ppm could be attributed to fluoride ions coordinated to hydroxide[74] or oxide species (Figure S5).[58] In addition, several of the spinning side bands for the $LiPF_6$ and LiF appear in this range, adding to the complexity of the spectrum.

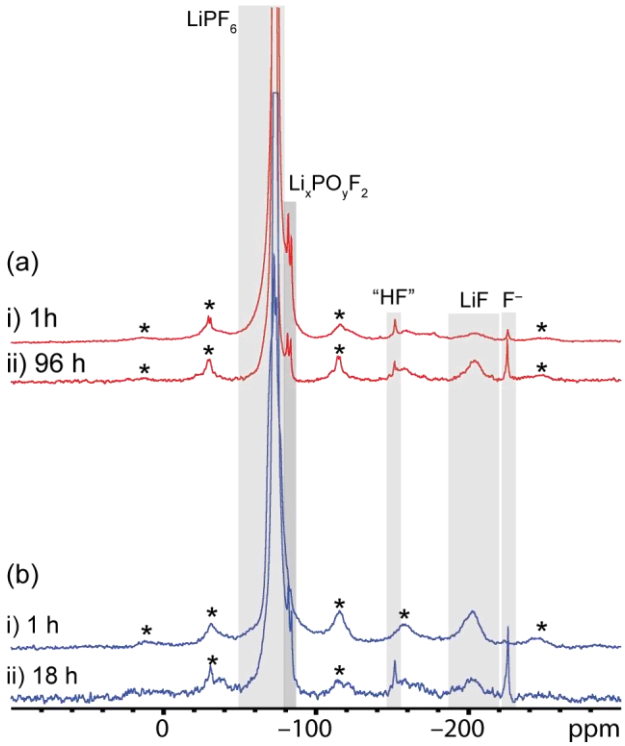

Figure S4. ^{19}F ssNMR of treated Cu flakes soaked in LP30 electrolyte. (a) d-HCl-Cu soaked for (i) 1 hour and (ii) 96 hours, (b) d-AcH-Cu soaked for (i) 1 hour and (ii) 18 hours. The spectra were acquired a MAS frequency of 25 kHz. The spinning side bands are marked with asterisks.

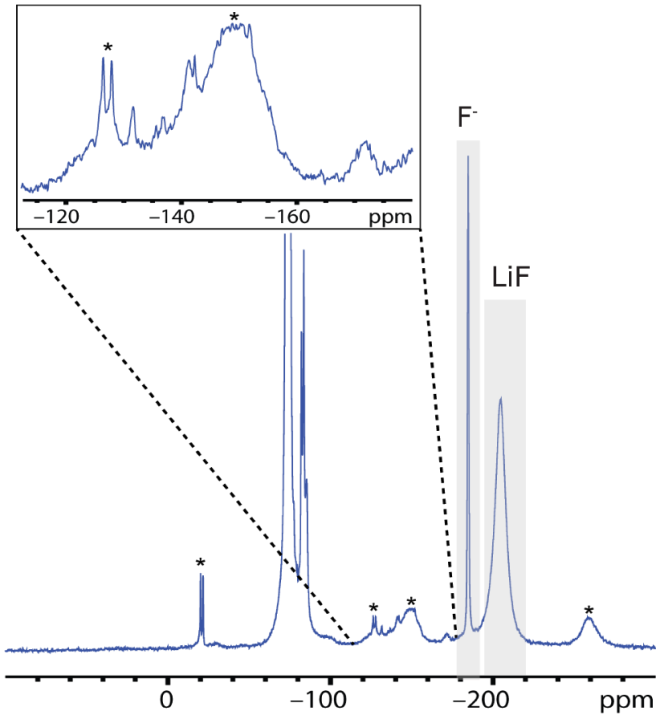

Figure S5. ^{19}F ssNMR of the N-SEI on d-AcH treated Cu soaked in LP30 for 24 hours. The spinning side bands are marked with asterisks. The spectra were acquired with a MAS frequency of 25 kHz.

The effect of N-SEI formation time is demonstrated for the N-SEI on d-HCl-Cu formed for 1 hour which gives rise to broader ^{7}Li resonance compared to that of the N-SEI formed for 96 hours (Figure S6).

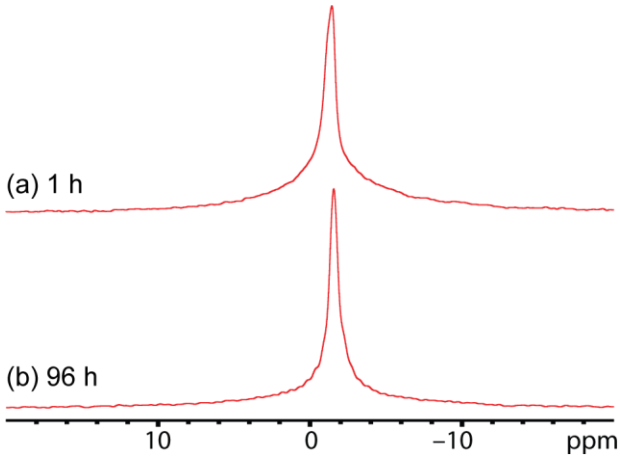

Figure S6. ^{7}Li ssNMR spectra of the N-SEI on d-HCl-Cu soaked in LP30 for (a) 1 hour and (b) 96 hours.

The resonances on all N-SEI were fitted with the combination of a broad and a narrow component, both having approximately the same isotropic chemical shift (Figure S7). The ^{7}Li NMR spectra for N-SEI on c-AcH-Cu powder is compared to those of the e-SEI pre-formed at

2 V, 1.4 V and 0.1 V voltage holds followed by lithium plating of 0.5 mAh cm^{-2} at 1.2 mA cm^{-2} on c-AcH-Cu and d-HCl-Cu (Figure S8(a) and (b), respectively). The e-SEI_{2v} gives rise to narrower ^{7}Li resonance compared to N-SEI for both samples. The ^{7}Li spectra of e-SEI on Cu were fitted with 2-3 components, mainly LiF (~ -1 ppm) and Li_2CO_3 (~ 0 ppm). Additional components with positive ^{7}Li shifts (~ 0.6, ~ 1.6, ~3 ppm) were assigned to LiOH, Li_2O_2 and Li_2O (Figure S9). [40,43]

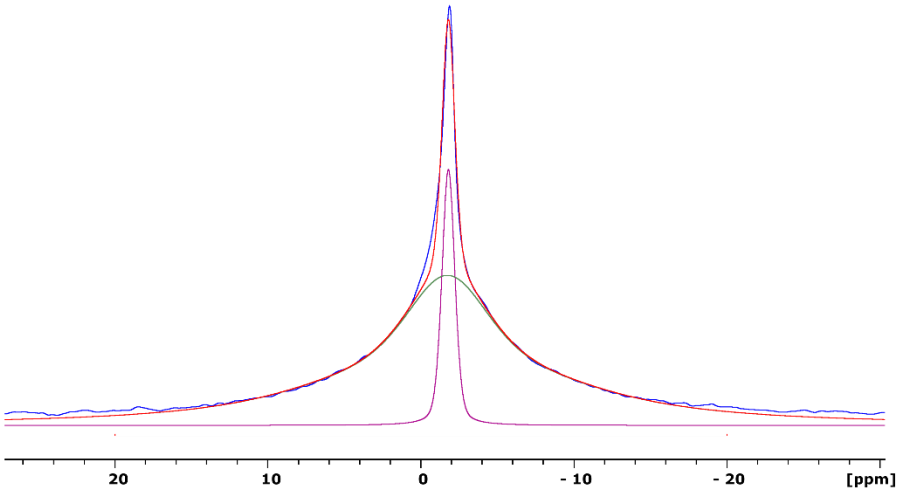

Figure S7. (a) Deconvoluted ^{7}Li ssNMR spectra of the c-AcH-Cu (flakes) soaked in LP30 for 18 hours (also shown in Figure 6). The fit consists of two components (a broad component at -0.5 ppm and a narrow component at -0.7 ppm).

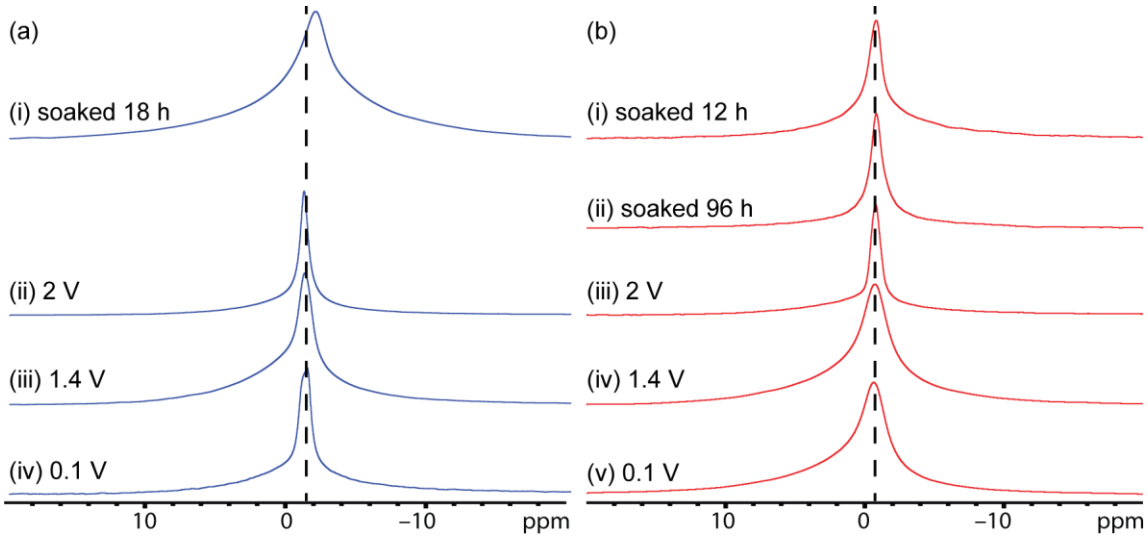

Figure S8. (a) ^{7}Li ssNMR of (i)c-AcH-Cu (flakes) soaked in LP30 for 18 hours, (ii) e-SEI_{2V}, (iii) e-$SEI_{1.4V}$ and (iv) e-$SEI_{0.1V}$ on lithium plated c-AcH-Cu (foil). (b) ^{7}Li ssNMR of d-HCl-Cu (flakes) soaked in LP30 for (i) 12 hours and (ii) 96 hours, (iii) e-SEI_{2V}, (iv) e-$SEI_{1.4V}$ and (v) e-$SEI_{0.1V}$ on lithium plated d-HCl-Cu (foil). The spectra were acquired with a MAS frequency of 25 kHz.

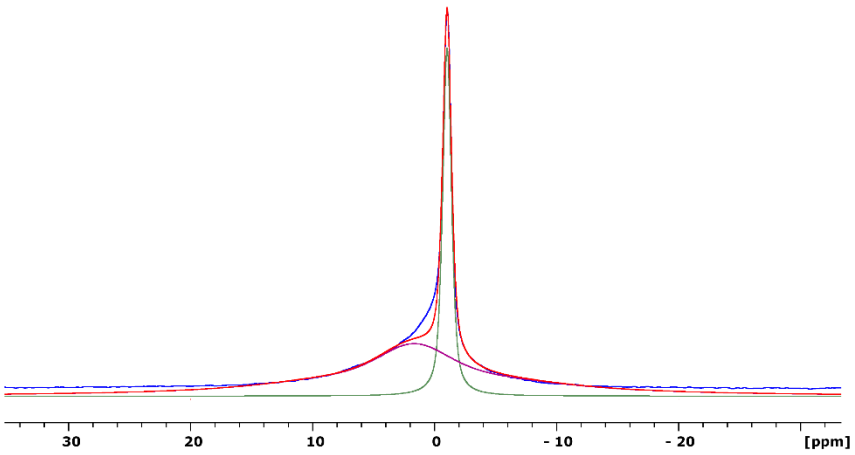

Figure S9. (a) Deconvoluted ^{7}Li ssNMR spectra of the e-SEI_{2V} (formed at 2 V for 45 hours) on lithium plated d-HCl-Cu (foil). The fit consists of two components (a broad component at 1.7 ppm and a narrow component at -1 ppm).

The ^{19}F NMR spectra of the scraped Li metal plated on to the c-AcH-Cu and d-HCl-Cu electrodes (with voltage hold of 2V for 10 and 24 hours on c-AcH-Cu and 12 and 70 hours on d-HCl-Cu) are depicted in Figure S10. In addition to the peaks corresponding to $LiPF_6$ and LiF, sharp resonances at -96 ppm (doublet) were observed for c-AcH-Cu sample soaked for 10

hours and sharp resonances at -142 ppm and -156 ppm were observed for the e-SEI_{2V} formed for 24 hours. In contrast, the LiF peak at -204 ppm and the -142 ppm resonances were absent from d-HCl-Cu spectra. For all e-SEI_{2V} samples, the resonance at -225 ppm was not observed (Figure S9), suggesting that this resonance is typical to N-SEI and that the assigned compound is consumed during polarization. The ^{19}F NMR spectrum of e-$SEI_{1.4V}$ on both d-HCl-Cu and c-AcH-Cu (Figure S10) consists of mainly $LiPF_6$ and LiF resonances.

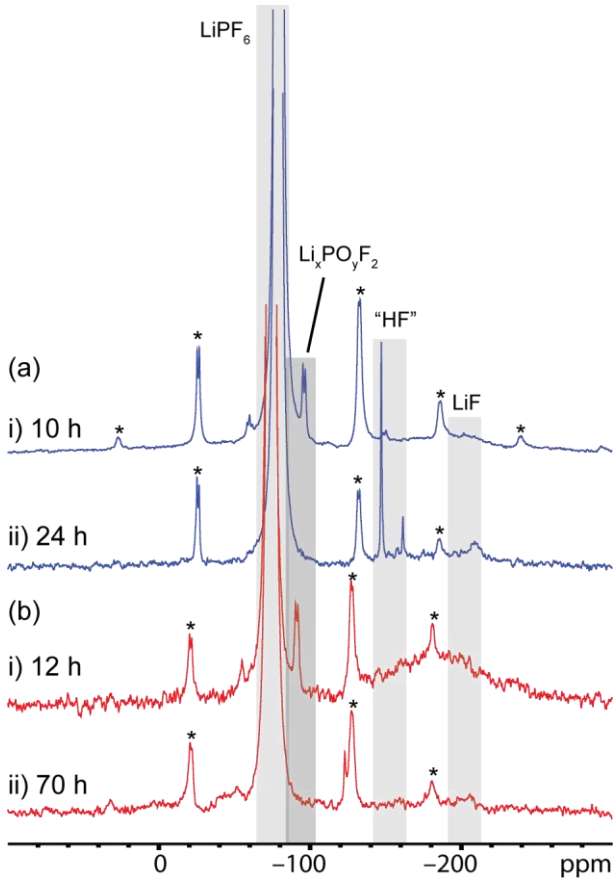

Figure S10. ^{19}F ssNMR of lithium microstructures plated on (a) c-AcH after SEI formation at 2 V in LP30 for (i) 10 hours and (ii) 24 hours (b) d-HCl-Cu after SEI formation at 2 V in LP30 for (i) 12 hours and (ii) 70 hours. Spinning side bands are marked with a star. The spectra were acquired with a MAS frequency of 25 kHz.

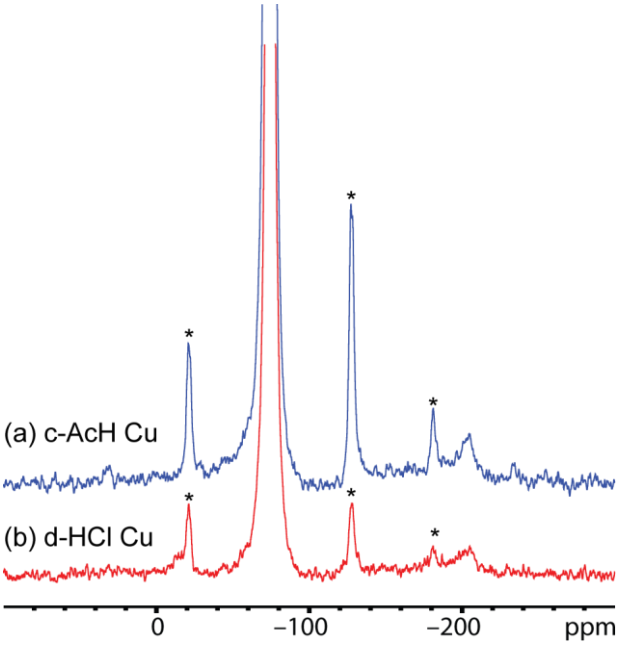

Figure S11. ^{19}F SSNMR spectra of e-SEI$_{1.4V}$ on lithium microstructures plated on (a) d-AcH-Cu after SEI formation at 1.4 V in LP30 for 80 hours and (b) d-HCl-Cu for 88 hours. Spinning side bands are marked with asterisks.

In order to establish whether the origin of the additional resonances is the Cu surface chemistry or the presence of lithium metal in the cell during the rest time, the ^{19}F NMR spectrum of Cu samples treated by both methods soaked either with or without a lithium disk in the coin cell were measured (Figure S12). The resonances were observed for d-HCl-Cu soaked in electrolyte regardless of the soaking time or presence of lithium metal (Figures 5, S10). Thus, these resonances could not be solely correlated to the treatment of the Cu or to the presence of lithium metal.

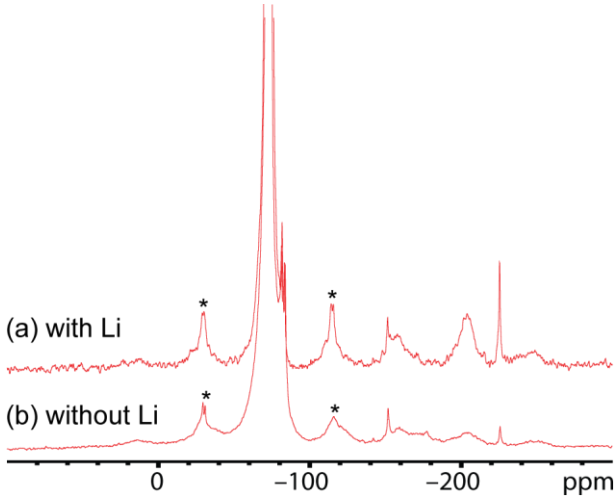

Figure S12. ^{19}F SSNMR spectra of N-SEI Cu-d-HCl soaked in LP30 for 96 hours (a) with lithium and (b) without lithium. Spinning side bands are marked with asterisks.

^{19}F NMR resonances in the range of -153 ppm to -159 ppm were assigned to HF. However, it is not fully clear how HF could exist in the solid phase and co-exist with Li metal (for the Li metal containing samples). A possible explanation could be that the origin for the HF signal is the hydrogen bond between OH^- ions and LiF on the Cu surface.[56,59,75–77]

XPS

The surface of d-HCl-Cu and c-AcH-Cu was studied by XPS. The d-HCl-Cu is characterized by a Cu metal and Cu(I) heterogeneous surface, while c-AcH-Cu is characterized by a mix of Cu(II) and Cu(I) oxides (Figures 4, S13). Since the Cu metal signal is less pronounced, the oxide coverage seems to be more homogeneous on c-AcH-Cu. Peaks at 931-932.4 eV (Cu 2p3/2) and 951.9-952.2 eV (Cu 2p1/2), observed in the Cu 2p spectrum and the O 1s peak at 530.2 eV are assigned to Cu metal and Cu(I) rich copper oxides, respectively (Figures S13-S14). The shoulder observed in the Cu 2p spectrum of c-AcH-Cu and the pristine copper current collector at 934-935 eV, the minor shake-up feature at 941-945 eV and the 531-531.2 eV peaks in the O1s spectrum serve as an indication for the presence of Cu(II) compounds, likely to be Cu(II) hydroxide. The typical Cu metal shoulder in the Auger spectrum (Figure S2b) of d-HCl-Cu serves as an evidence for the more heterogeneous thickness of the oxide layer on d-HCl-Cu, compared to c-AcH-Cu and pristine non-treated Cu metal. The SEI formed on the surface of d-HCl-Cu was chosen to be studied since d-HCl pre-treatment is a typical preparation procedure for copper current collectors in the literature.

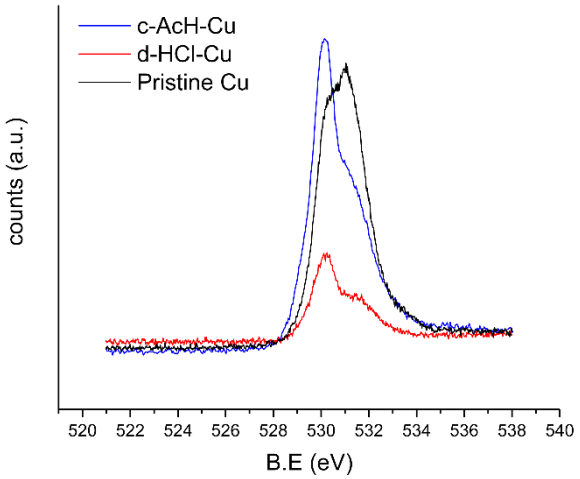

Figure S13. O 1s XPS spectrum of pristine (black), HCl treated (red) and acetic acid treated (blue) copper current collectors.

The peaks at 932 eV ($Cu2p_{3/2}$) and 951.75 eV ($Cu2p_{1/2}$) were observed in the Cu 2p XPS spectra of N-SEI, e-SEI_{2V} and d-HCl-Cu foil (Figure S14). These peaks are typical to the spectrum of Cu metal and Cu_2O. In addition, a slight shoulder at 934-935 eV was observed for e-SEI_{2V}, it can be assigned to $Cu(OH)_2$. The minor shake-up feature at 941-945 eV, indicating the presence of Cu(II) compounds, suggests further reactivity of the Cu compounds during SEI formation around 2V.

The Cu 2p spectrum for e$SEI_{1.4V}$ (Figure S15) is significantly different; no Cu 2p peaks were observed measuring the surface of this sample. After 10 nm sputtering peaks at 932.0 eV (Cu $2p_{3/2}$) and 952 eV (Cu $2p_{1/2}$) appeared. This spectrum is very similar to that recorded for the N-SEI and eSEI_{2V} and could suggest that applying 1.4 V constant voltage gives rise to a thicker SEI. Further sputtering of an additional 10 nm gives rise to negative shift of both peaks (931.5, 951.35 eV) indicating possible Cu oxide lithiation or the formation of Cu nanoparticles. [51,78]

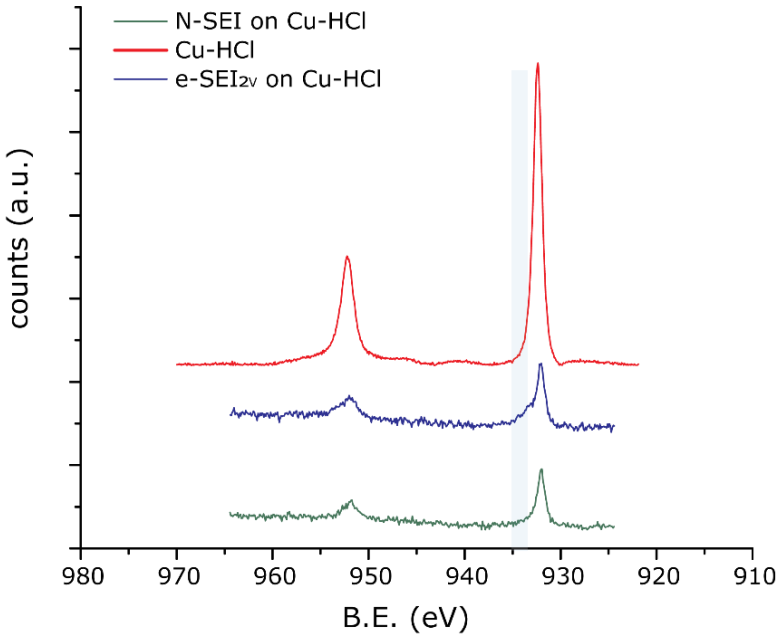

Figure S14. Cu 2p XPS spectrum of d-HCl-Cu (red), N-SEI on d-HCl-Cu (green) and $eSEI_{2V}$ d-HCl-Cu (blue).

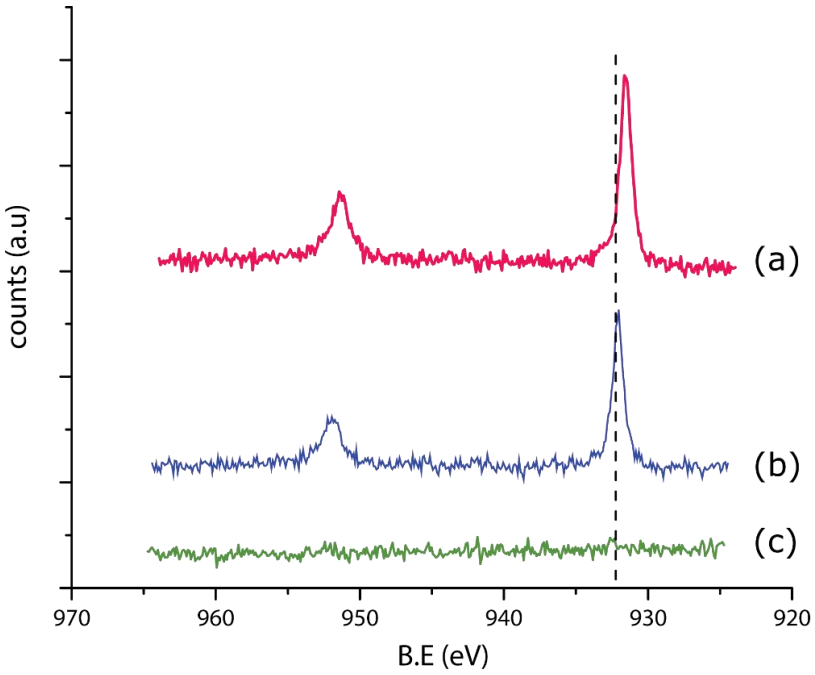

Figure S15. Cu 2p XPS spectrum of $eSEI_{1.4V}$ on d-HCl-Cu surface (c), 10 nm sputtering (b) and 20 nm sputtering (a). The black line is placed for visual reference to the binding energy shift upon sputtering.

The C 1s spectrum of N-SEI includes peaks at 286.4 eV (C-O) and 288.7 eV (C=O) as a result of solidified ethylene carbonate (Figure S16a). The corresponding O 1s spectrum is deconvoluted to two peaks at 532 eV (C=O) and 533.4 (C-O) (Figure S16b). Since EC

solidification occurred during sample preparation, it should not be considered as a component of the N-SEI. The O 1s peak around 532 eV could also have a contribution from oxygen atoms in Cu oxides and phosphates (P-O) which result from the decomposition of the $LiPF_6$ salt. The presence of phosphates is further supported by the P 2p signal around 132-140 eV assigned to $Li_xPO_yF_z$ (Figure S17). [36] The broad lithium peak around 56 eV indicates the presence of $LiPF_6$ along with its decomposition products (Li_xPF_y, $Li_xPO_yF_z$) and LiF (Figure S16d) which is also in corroboration with the presence of F1s peaks at 685.3 eV (typical for LiF) and 687.2 eV (typical for $LiPF_6$ decomposition products) (Figure S16c) [17]. These findings suggest that the N-SEI on Cu is composed of Cu oxides and the $LiPF_6$ decomposition products also seen in the ^{19}F NMR.

The XPS C 1s, O 1s, F1s and Li1s spectra of e-SEI_{2V} are very similar to the spectra recorded for the N-SEI (Figure S16). However, the C1s spectrum shows an increase in the intensity of C-O and C=O components in comparison to C-C/C-H components (Figure S16). In addition, the increase in the intensity of the P 2p peak (Figure S17) at 135 eV suggests the simultaneous formation of phosphates [36] and polymeric phosphorous containing PEO-like compounds at 2 V. [38]

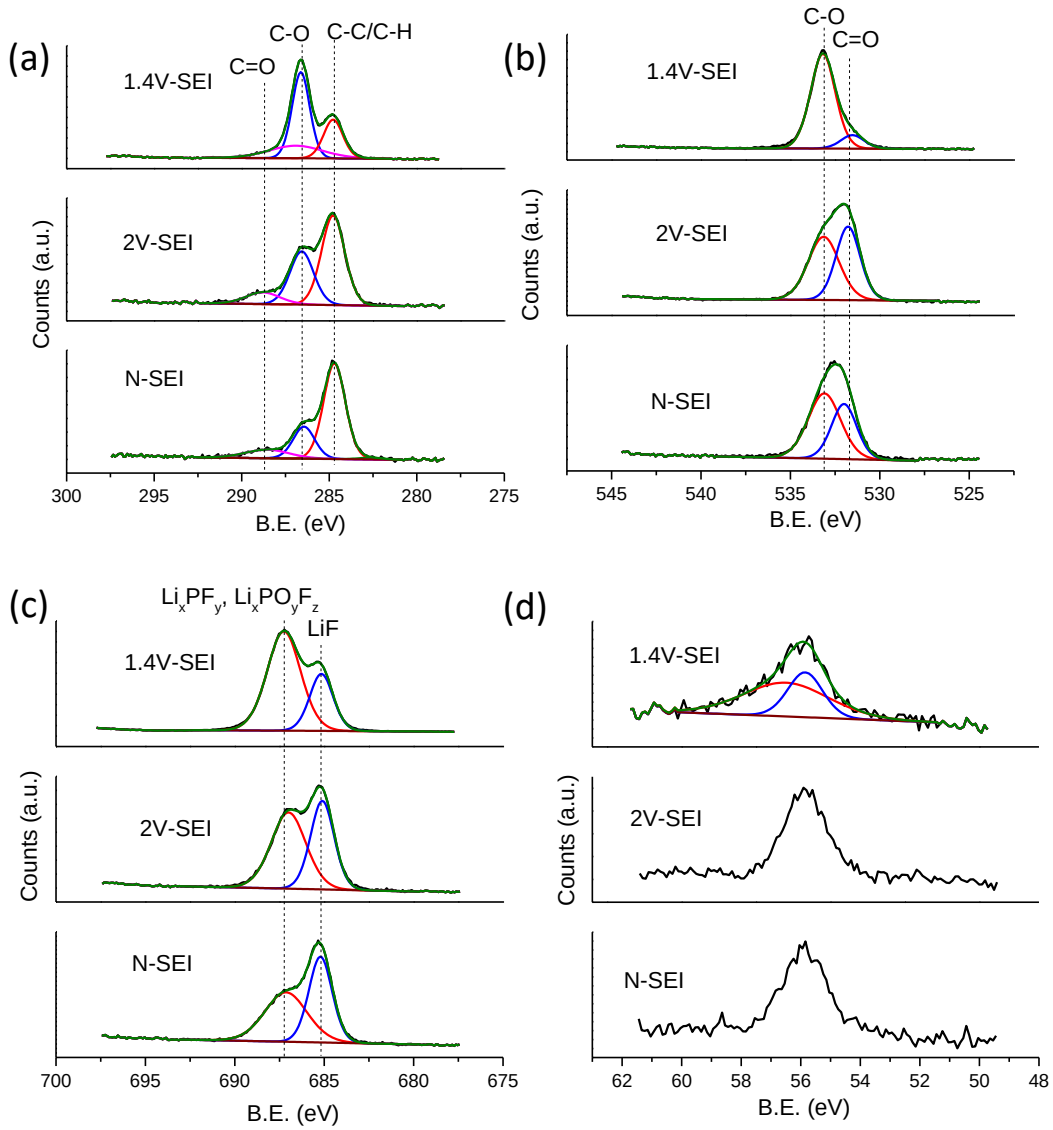

Figure S16. (a) C 1s (b) O 1s (c) F 1s and (d) Li 1s XPS spectra of N-SEI (bottom), $eSEI_{2V}$ (middle) and $eSEI_{1.4V}$ (top). The recorded and final resultant fitted curves are plotted in black and green colours respectively. The components spectra are shown in blue, red and magenta colours.

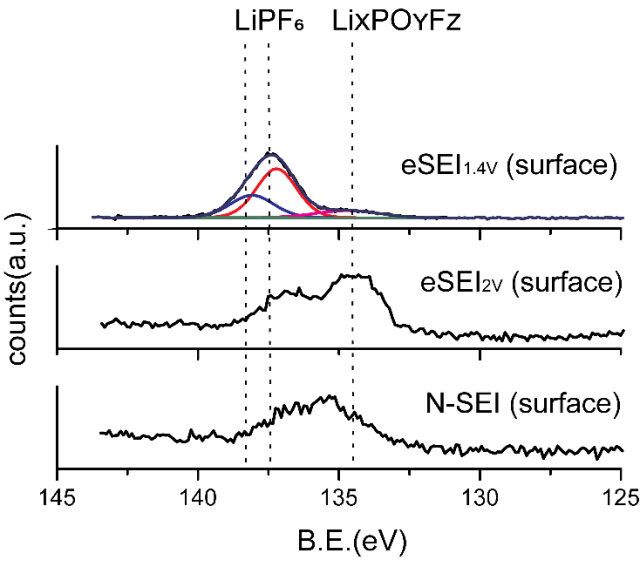

Figure S17. P 2p spectrum of N-SEI (bottom), $eSEI_{2V}$ (middle) and $eSEI_{1.4V}$ (top). The recorded and final fitted curves are plotted in black and green colours respectively. The components spectra are shown in blue, red and magenta colours.

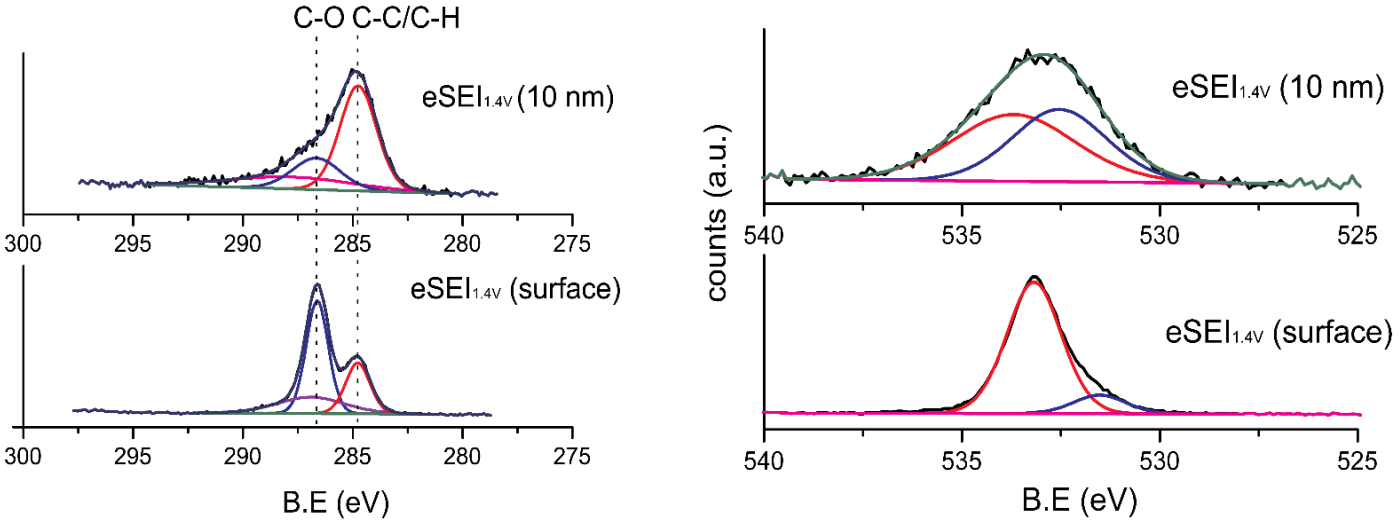

Figure S18. C 1s (left) and (b) O 1s (right) XPS spectrum of 1.4 V-SEI before and after 10 nm sputtering.

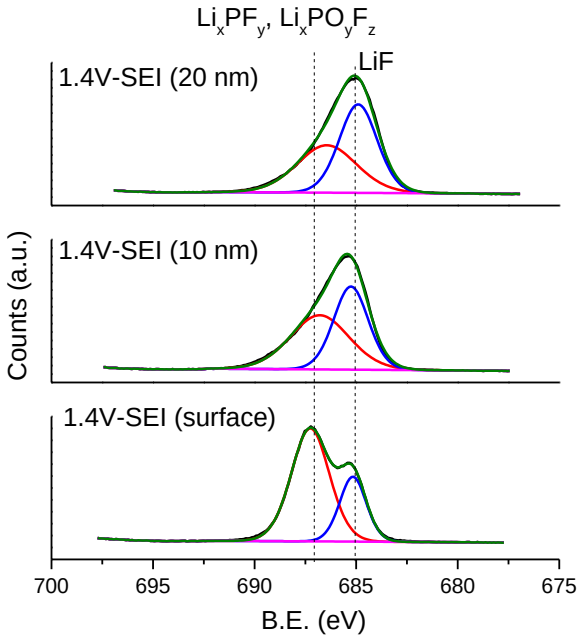

Figure S19. F 1s XPS spectrum of 1.4 V-SEI before and after 10 and 20 nm sputtering.

Table S2. Florine containing components composition as function of sputtering depth in e-SEI$_{1.4V}$

	Li_xPF_y or Li_XPO_yF (%)	LiF (%)	LiF / Li_xPF_y or Li_XPO_yF ratio
Surface	71.3	28.7	0.4
10 nm	52.5	47.5	0.9
20 nm	45.7	54.3	1.18

The composition of the SEI on lithium plated Cu substrates was studied with XPS both on the plated lithium and on the surface of the exposed Cu SEI areas (Figures S20-22). Similarly to the e-SEI$_{1.4V}$ (Figure S15), the Cu 2p signals were not observed on the surface, presumably since the SEI on the lithium plated sample is thicker and the Cu compounds are buried deeper than 20 nm (Figure S20). After sputtering 20 nm of the exposed Cu area, the Cu 2p spectrum was observed with more significant negative shifts (929.74 eV and 949 eV), this could be due to both or either Cu oxide lithiation and Cu metal nano-cluster formation. [25,36,51,78] Sputtering of 20 nm of the lithium-plated area did not give rise to any Cu 2p peaks (Figure S20).

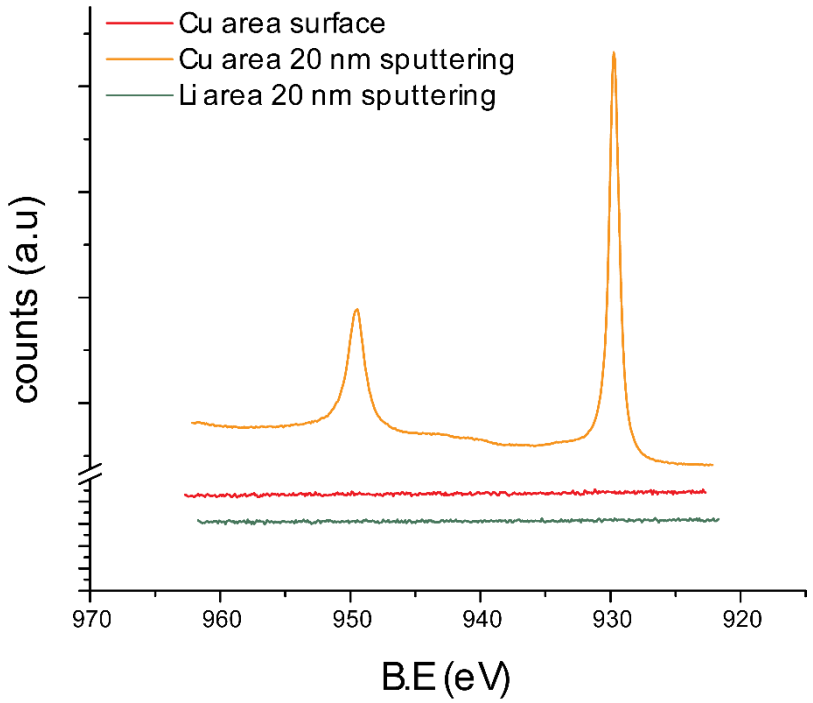

Figure S20. Cu 2p XPS spectrum of SEI on lithium plated d-HCl-Cu surface (non-plated area) (red), 20 nm sputtering (orange) and 20 nm sputtered lithium plated area (green).

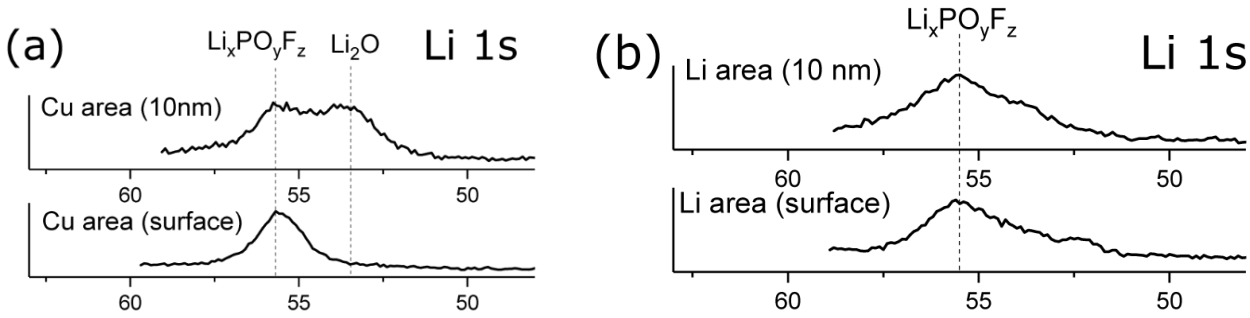

Figure S21. Li 1s XPS spectra of SEI on Li (a) and Cu (b) areas on plated d-HCl-Cu area.

In situ NMR

The skin depth of Li metal in this study is $d = \sqrt{\frac{\rho}{\pi \mu_0 \mu_r \nu}}$ = 12.1 μm where ρ is the resistivity of the metal (94.7 n Ω for Li metal at 298 K), μ_0 is the permeability of the vacuum ($4\pi\ 10^{-7}$ m kg/ s^2A^2), μ_r is the relative permeability of the medium (μ_r = 1.4 for Li metal) and ν is the frequency of the applied rf field (116.7 MHz).[81,82]

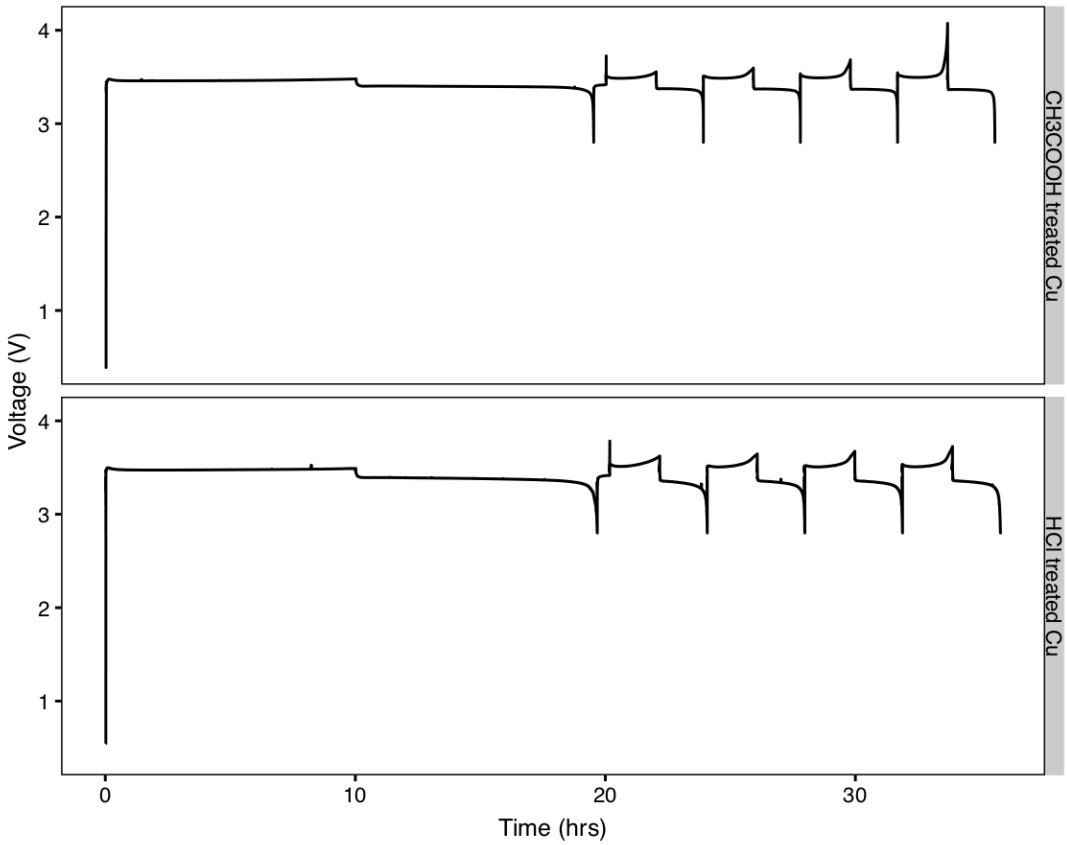

Figure S22. Galvanostatic cycling of in situ Cu-LFP cells with a) c-AcH-Cu and b) d-HCl-Cu where 0.01 mA/cm^2 was used for the first cycle and 0.5 mA/cm^2 for the subsequent cycles. The equivalent charge of 1 mAh/cm^2 was passed.

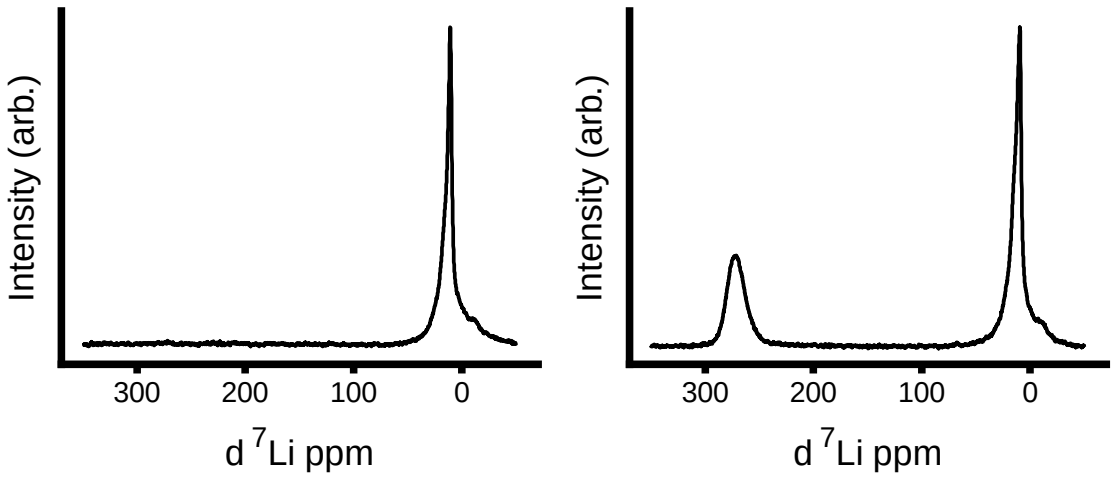

Figure S23. a) The ^{7}Li in situ NMR spectra at the start of cycling where only the diamagnetic peak originating from the electrolyte is observed. b) The ^{7}Li in situ NMR spectra at the end of charge (1 mAh/cm^2) showing both the Li metal peak centered around approximately 260 ppm and the electrolyte peak.

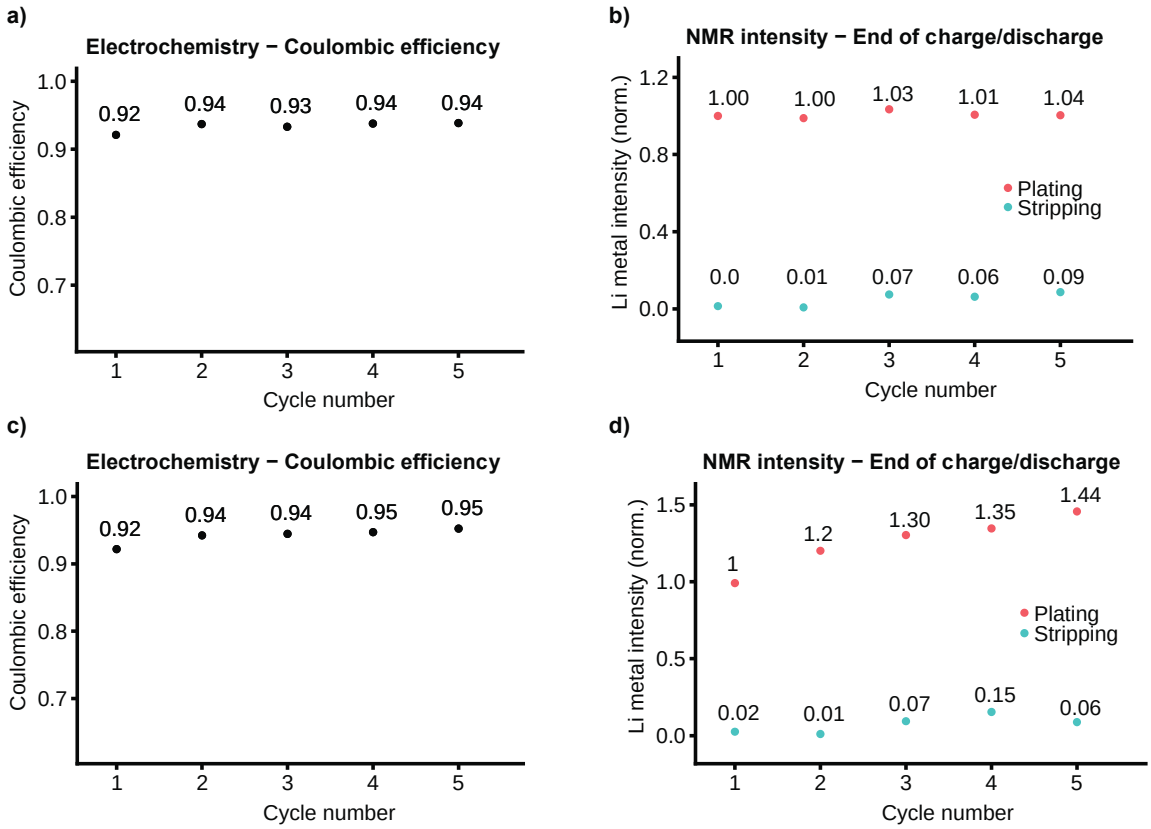

Figure S24. a) The coulombic efficiency (CE) of the galvanostatic cycling performed in in situ NMR cells and the corresponding normalized intensity of the Li metal peak quantified with in situ NMR at the end of charge (plating) and discharge (stripping) for a-b) c-AcH-Cu and c-d) d-HCl-Cu. The CE and the amount of dead Li quantified with NMR (the intensity of Li metal at the end of discharge) is similar for both surface treatments whereas the intensity of Li metal at the end of charge is different for the two cells.

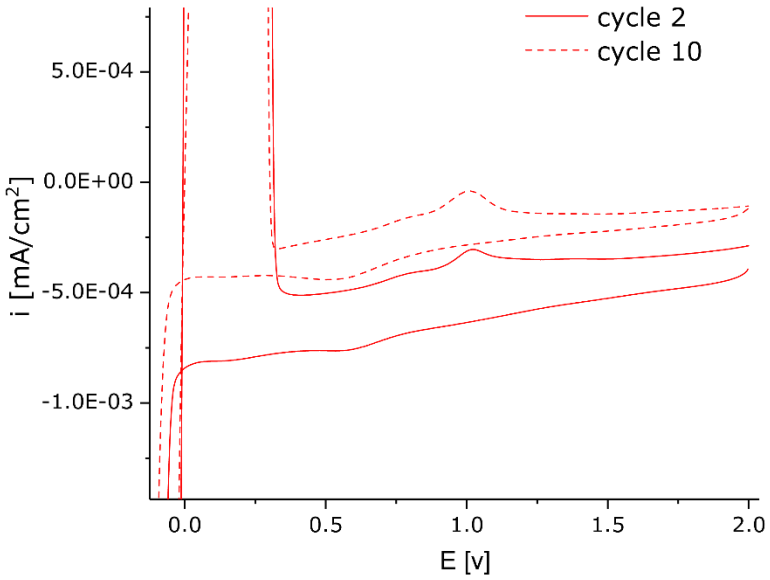

Figure 25. 2nd (full line) and 10th (dashed line) cycle CV of lithium plating on d-HCl-Cu in three-electrode cell, Cu WE vs. Li disk CE and RE, with scan rate 1mV/sec

TOF-SIMS

The measurements were conducted in the burst alignment mode (BAM) for better lateral resolution of images with a Bi^+ primary beam (25 keV) and a Cs^+ sputtering beam (500 eV) over an area of 250 µm × 250 µm (sputtering area 500 µm × 500 µm). During the measurements, the current for the sputtering beam was steady and constant (35 nA), thus over the same sputtering span, the fluence dose density were expected to be the same for all the samples. Moreover, the high current bunch mode (HCBM) with a mass resolution up to 10000 was also applied to ensure that within the limitation of the instrument, the species analysed in BAM mode were solely contributing. For these air sensitive samples, they were mounted inside an Ar-filled glovebox and transferred into the instrument within the vacuum transport suitcase which was opened until the pressure of the loadlock chamber lower than 10^{-5} mbar.

The intensity of different species in SIMS are affected by a variety of different factors and the concentration of species normally cannot be obtained directly from the intensity data. However, for the same species, assuming the chemical environment was similar within the same sample and among samples with similar treatments, the relative intensities correlated with related concentrations are comparable.

Native and electrochemical SEI on Cu were studied by ToF-SIMS. Cu_xO, LiF, CuF_x and OH^--related species were observed in N-SEI and e-SEI at all tested conditions. Since the penetration depth of the SIMS is on the order of the thickness of N-SEI and constant-voltage e-SEI, the acquired depth profiles were analysed qualitatively.

In Figure S26 the depth profiles of the copper metal (detected as Cu_2^-) on N-SEI or e-SEI are depicted. The sharp increase of the copper metal signal (detected as Cu_2^-) served as an indication of the end of SEI sputtering (Figure S26). The thickness of the N-SEI is lesser than the penetration depth of the ToF-SIMS experiment, thus the copper metal intensity increases immediately at the start of sputtering, while the e-SEI is thicker and as a result the intensity increase occurs after a lag. The sharp increase in the Cu metal signal occurs after longer sputtering for the N-SEI and e-SEIs on c-AcH-Cu, thus the SEIs formed on c-AcH-Cu are thicker compared to the ones on d-HCl-Cu.

Depth profiles of Cu oxides by using SIMS (Figure S26) suggest that the SEI formed on c-AcH-Cu is thicker than the SEI on d-HCl-Cu. LiF depth profiles (Figure S27a) indicates that LiF forms mainly during rest at open circuit voltage (OCV) and at reduction potentials above 2 V.

(a) (b)

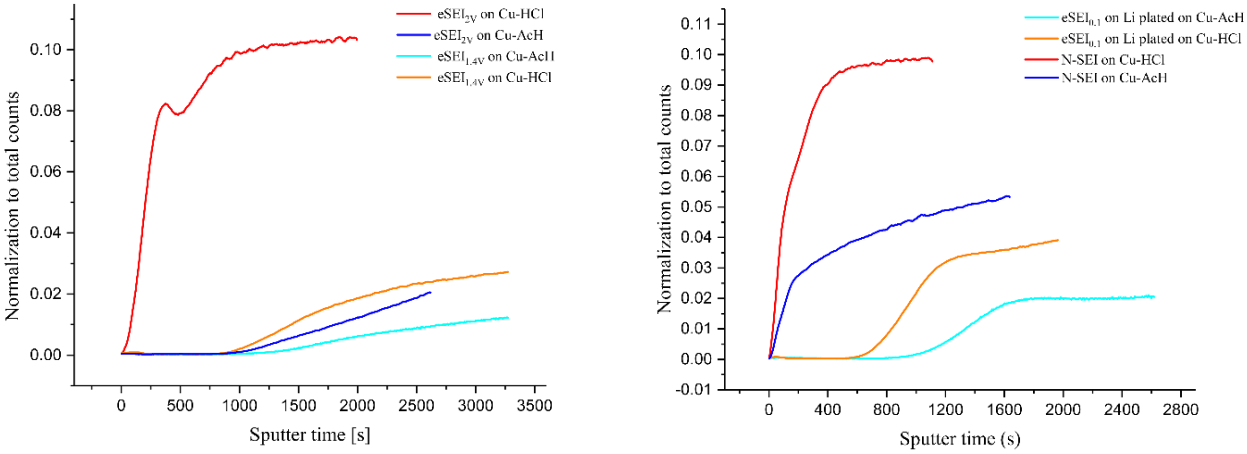

Figure S26. (a) Cu metal depth profile of N-SEI and $eSEI_{0.1V}$ and on lithium plated copper (b) $eSEI_{1.4V}$ and $eSEI_{2V}$ on copper

Lithium fluoride (LiF, detected as LiF_2^-) depth profiles on d-HCl-Cu are presented in Figure S27a. The LiF intensity is significantly higher for the high voltages (2 and 2.8 V) compared to N-SEI (rest) and the low voltage steps (1.4 V and 0.1 V). This suggests that most of the LiF forms at high voltages (i.e., 2 and 2.8 V). The LiF depth profile in N-SEI on d-HCl-Cu vs c-AcH-Cu (Figure S27c) further supports thicker N-SEI on c-AcH-Cu.

The depth profiles of $^{65}CuO^-$ in N-SEI on d-HCl-Cu and c-AcH-Cu are depicted in Figure S14b. Copper fluorides (detected as $^{65}CuF_2^-$) were observed in N-SEI and SEI on copper by TOF-SIMS (Figure S27b). The CuF_2 depth profile of N-SEI and SEI reveals similar behaviour to copper oxides. Moreover, CuF_2 was observed in the XPS spectra. F1s gives rise to a broad peak for CuF_2 around 685 eV, however this peak overlaps with LiF. Copper fluorides were not found by ssNMR, this is probably because CuF_2 contains paramagnetic Cu(II) that is not visible to ssNMR.

(a)

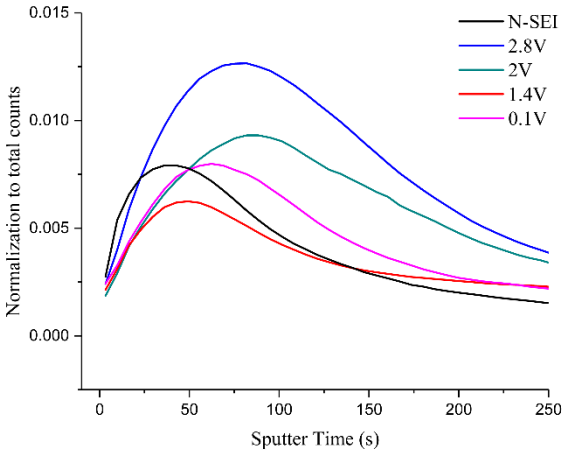

(b)

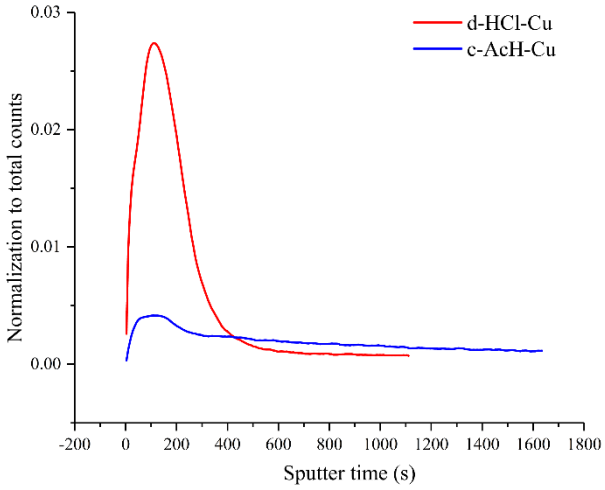

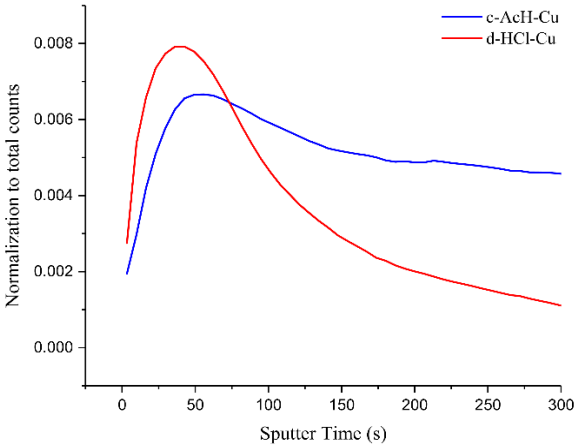

(c)

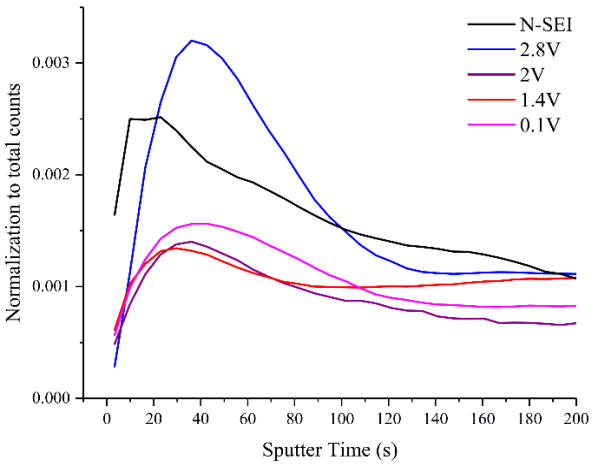

(d)

Figure S27. (a) LiF (LiF_2^-) depth profile in constant-voltage and N-SEI on d-HCl-Cu. (b) ^{65}CuO depth profile in N-SEI on d-HCl-Cu and c-AcH-Cu. (c) LiF depth profile in N-SEI on d-HCl-Cu (red) and c-AcH-Cu (blue). (d)CuF_2 ($^{65}CuF_2$) depth profile in e-SEI formed at 0.1,1.4,2,2.8 V on d-Cu-HCl. The presented profiles were limited to the sputtering time at which the Cu metal signal intensity increased abruptly.

The presented ToFSIMS depth profiles are the results of signal collection from the analysis area (250 µm × 250 µm).However, further data analysis of the ^{65}CuO signal from different regions of interest, i.e. the exposed copper and plated lithium, confirmed the presence of copper oxides in the SEI on both areas. The calculated thickness of the plated lithium is approximately 1 µm assuming 70% efficiency and coverage of 50% of the copper area. Thus, it is assumed that for all the SIMS analysis, the copper oxides remaining on the underlying copper substrates cannot contribute to the copper oxide signals recorded from the lithium surface.

The 3D reconstruction of $^{65}CuO^-$ signal (XZ plane) of $eSEI_{0.1V}$ on lithium platted d-HCl-Cu (right) and c-AcH-Cu (left) in depicted in Figure S28. For each sample the $^{65}CuO^-$ signals for SEI on lithium and the exposed Cu are compared. The intensity of $^{65}CuO^-$ in the SEI on the exposed d-HCl-Cu is higher compared to the exposed c-AcH-Cu and that the increase of $^{65}CuO^-$ signal with sputtering is more gradual on d-HCl-Cu. The intensity of the $^{65}CuO^-$ signal from the SEI on the plated lithium is similar to the signal from the top layers of he SEI on the exposed copper.

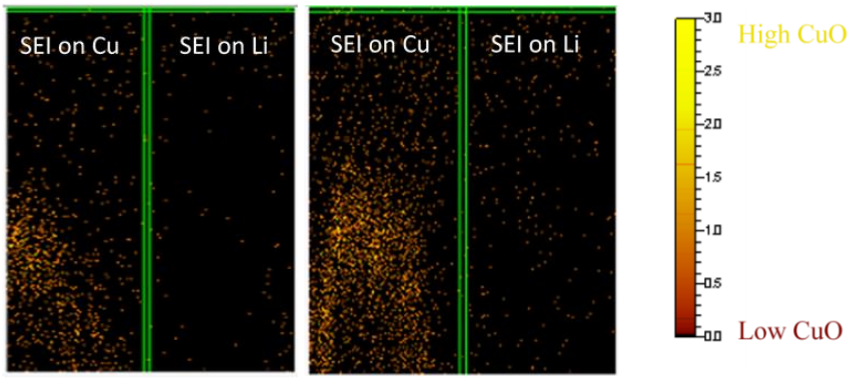

Figure S28. 3D reconstruction of ^{65}CuO signal (XZ plane), comparing the intensity of ^{65}CuO on exposed and lithium plated areas on a copper disk after the application of lithium plating procedure (d-HCl-Cu-right, c-AcH-Cu- left).

Lithium plating on Cu

The XY maps of OH^- and LiF (detected as LiF_2^-) in the $eSEI_{0.1v}$ on c-AcH-Cu (Figure S29), LiF and OH^- XY and XZ maps of $eSEI_{2V}$ on c-AcH-Cu (Figure S30) and d-HCl-Cu (Figure S31) reveal a similar trend to the SEI composition trend on d-HCl-Cu (Figure 10).

(a) (b)

Figure S29. XY (total) OH^- (a) and LiF (LiF_2^-) (b) maps of $eSEI_{0.1V}$ on c-AcH-Cu.

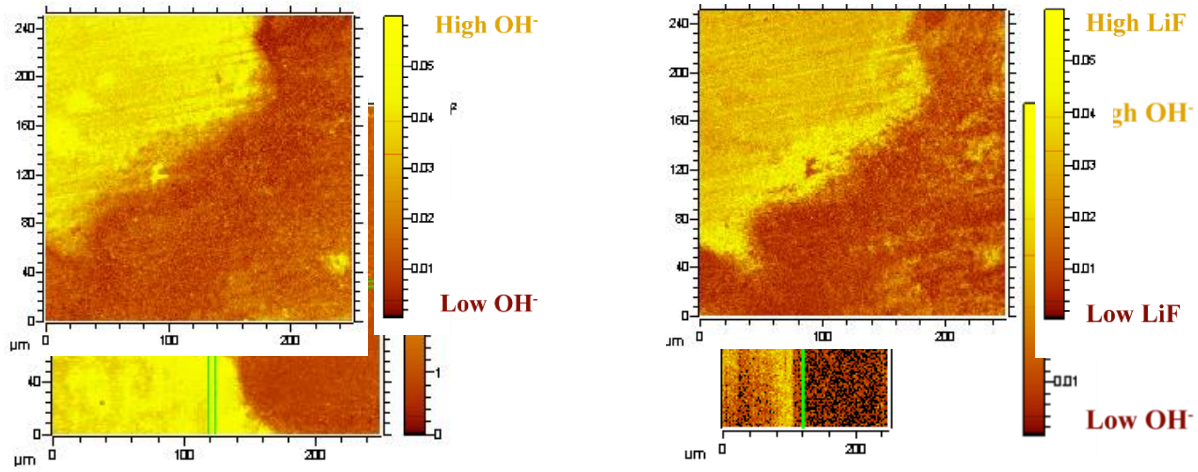

(a) (b)

Figure S30. XY (total) (a) and XZ (5 layers) (b) maps of OH^- on $eSEI_{2V}$ on c-AcH-Cu.

(a) (b)

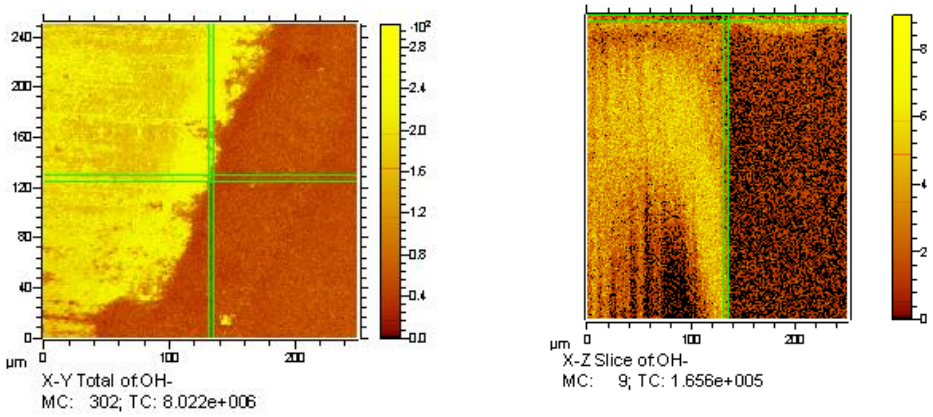

Figure S31. XY (total) (a) and XZ (5 layers) (b) maps of OH^- on $eSEI_{2V}$ on d-HCl-Cu, recorded on both lithium-plated and bare regions with equal sizes areas of 50X50 µm.

(a) (b)

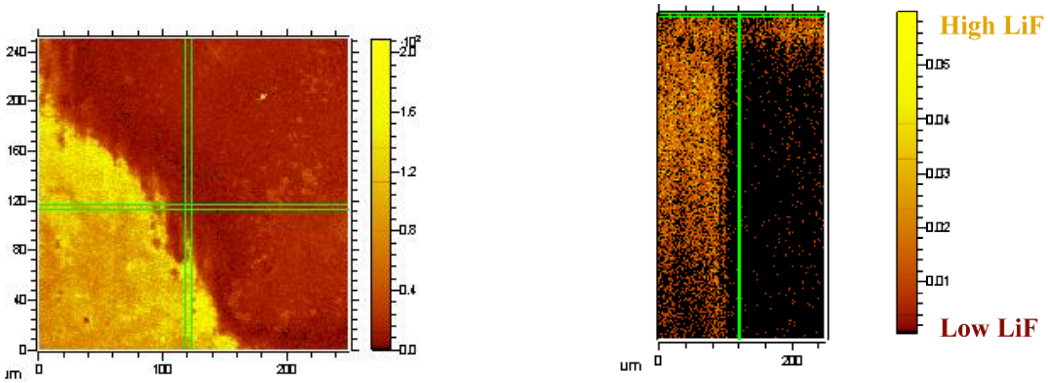

Figure S32. XY (total) (a) and XZ (5 layers) (b) maps of LiF (LiF_2^-) on $eSEI_{2V}$ on c-AcH-Cu.

(a) (b)

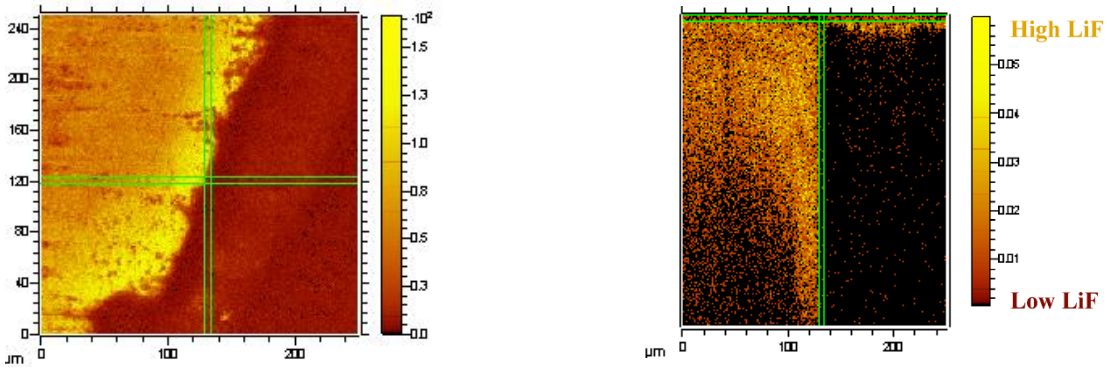

Figure S33. XY (total) (a) and XZ (5 layers) (b) maps of LiF (LiF_2^-) on $eSEI_{2V}$ on d-HCl-Cu .

OH^- depth profiles of N-SEI on d-HCl-Cu and c-AcH-Cu samples, (Figure S34). The OH^- intensity in N-SEI on d-HCl-Cu is higher. The intensity of the OH^- signal for the N-SEI on d-

HCl-Cu is significantly higher and more heterogeneous compared to that of N-SEI on c-AcH-Cu. These findings strengthen the reliability of the OH^- mapping and support the assumption of preferential plating on OH^- poor areas.

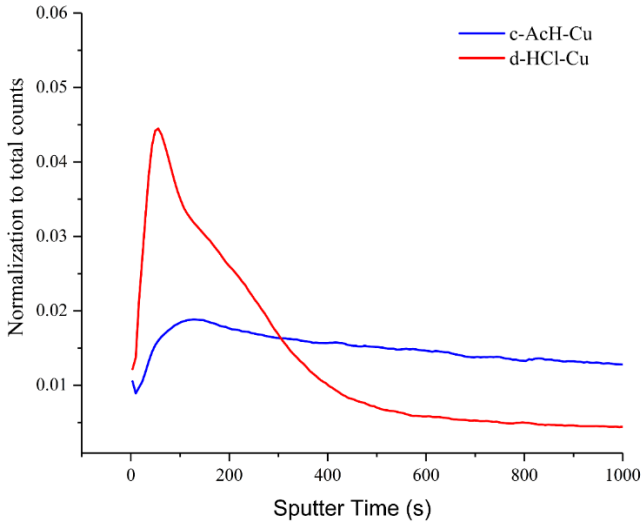

Figure S34. OH^- depth profile in SEI formed at N-SEI Normalised to total counts

Additional terms and definitions

Throwing power- the improvement in the distribution of the deposit resulting from the differing resistances between the anode and various portions of the cathode and the consequent variation of current density over the surface. [83]

	Energy [eV]	Assignment	Reference
C 1s	282.15	Li_2C_2	[17]
	284.4-284.8	C-C, C-H	[17]
	286.4-286.6	C-O-C, PEO, $(CH_2OCO_2Li)_2$	
	288.7-288.8	C=O	
	288.8-289.3	CO_3^-	
O 1s	528	Li_2O	[17]
	531	LiOH or H_2O_{ad}	[47,17]
	531.2	P=O or Li_2O_2	
	531.7	LiOH or H_2O_{ad}	
	532-532.6	P-O or C=O	[28]
	533.5	PEO, C-O	[17]
Cu 2p	929.7-931.5, 949-951.35	Li_xCuO or Cu np	[37,60,36,28,61]
Cu 2p	932, 951.75	Cu, Cu(I)	
Cu 2p	934-935	Cu (II) in $Cu(OH)_2$	
Li 1s	53-54	Li_2O	
	56	Li_xPFy, $Li_xPO_yF_z$	[36,17,50]
F 1s	685.3	LiF	[17]
F 1s	687.2-687.3	$LiPF_6$	[17]
P 2p	135	Phosphates	

Table S2. C1s, O1s, F1s, Li1s, P2p and Cu2p peak energies used for the XPS analysis

Compound	Detected as	Mass
LiF	$Li_2F_3^-$	71.0280
LiF	LiF_2^-	45.0132
Cu_xO	$^{65}CuO^-$	80.9233
Cu metal	Cu_2^-	125.8598
OH^-	OH^-	17.0033

Table S3. main compounds observed in TOFSIMS analysis

References

1. Liu, J. *et al.* Pathways for practical high-energy long-cycling lithium metal batteries. *Nat. Energy* **4**, 180–186 (2019).

2. Qian, J. *et al.* Anode-Free Rechargeable Lithium Metal Batteries. *Adv. Funct. Mater.* **26**, 7094–7102 (2016).

3. Neudecker, B. J., Dudney, N. J. & Bates, J. B. 'Lithium-free' thin-film battery with in situ plated Li anode. *J. Electrochem. Soc.* **147**, 517–523 (2000).

4. Schmitz, R. *et al.* SEI investigations on copper electrodes after lithium plating with Raman spectroscopy and mass spectrometry. *J. Power Sources* **233**, 110–114 (2013).

5. Menkin, S., Golodnitsky, D. & Peled, E. Artificial solid-electrolyte interphase (SEI) for improved cycleability and safety of lithium-ion cells for EV applications. *Electrochem. commun.* **11**, (2009).

6. Peled, E. & Menkin, S. Review — SEI : Past , Present and Future. *J. Electrochem. Soc.* **164**, (2017).

7. Li, Q. *et al.* Homogeneous Interface Conductivity for Lithium Dendrite-Free Anode. *ACS Energy Lett.* **3**, 2259–2266 (2018).

8. Hao, F., Verma, A. & Mukherjee, P. P. Mechanistic insight into dendrite-SEI interactions for lithium metal electrodes. *J. Mater. Chem. A* **6**, 19664–19671 (2018).

9. Myung, S. T., Sasaki, Y., Sakurada, S., Sun, Y. K. & Yashiro, H. Electrochemical behavior of current collectors for lithium batteries in non-aqueous alkyl carbonate solution and surface analysis by ToF-SIMS. *Electrochim. Acta* **55**, 288–297 (2009).

10. Kitz, P. G., Lacey, M. J., Novák, P. & Berg, E. J. Operando EQCM-D with Simultaneous in Situ EIS: New Insights into Interphase Formation in Li Ion Batteries. *Anal. Chem.* **91**, 2296–2303 (2019).

11. Lin, D. *et al.* Fast galvanic lithium corrosion involving a Kirkendall-type mechanism. *Nat. Chem.* **11**, 382–389 (2019).

12. Huang, W. *et al.* Nanostructural and Electrochemical Evolution of the Solid-Electrolyte Interphase on CuO Nanowires Revealed by Cryogenic-Electron Microscopy and Impedance Spectroscopy. *ACS Nano* **13**, 737–744 (2019).

13. Guidotti, R. A. & Nelson, G. C. PASSIVE-FILM FORMATION ON METAL SUBSTRATES IN IM LiPF/EC-DMC SOLUTIONS RONALD. *Mat. Res. Soc. Symp. Proc.* **496**, 469–475 (1998).

14. Andersson, A. M., Henningson, A., Siegbahn, H., Jansson, U. & Edström, K. Electrochemically lithiated graphite characterised by photoelectron spectroscopy. *J. Power Sources* **119**–**121**, 522–527 (2003).

15. Goh, S. W., Buckley, A. N., Skinner, W. M. & Fan, L.-J. An X-ray photoelectron and absorption spectroscopic investigation of the electronic structure of cubanite, CuFe2S3. *Phys. Chem. Miner.* **37**, 389–405 (2010).

16. Fiedler, C., Luerssen, B., Rohnke, M., Sann, J. & Janek, J. XPS and SIMS analysis of solid electrolyte interphases on lithium formed by ether-based electrolytes. *J. Electrochem. Soc.* **164**, A3742–A3749 (2017).

17. Eshetu, G. G. *et al.* In-Depth Interfacial Chemistry and Reactivity Focused Investigation of Lithium-Imide- and Lithium-Imidazole-Based Electrolytes. *ACS Appl. Mater. Interfaces* **8**, 16087–16100 (2016).

18. Jung, E. Y. *et al.* Experimental study on solid electrolyte interphase of graphite electrode in Li-ion battery by surface analysis technique. *Mol. Cryst. Liq. Cryst.* **663**, 158–167 (2018).

19. Hua, X. *et al.* Comprehensive study of the CuF2 conversion reaction mechanism in a lithium ion battery. *J. Phys. Chem. C* **118**, 15169–15184 (2014).

20. Novák, P. CuO cathode in lithium cells-III. Its discharge kinetics. *Electrochim. Acta* **31**, 1167–1173 (1986).

21. Novák, P. CuO cathode in lithium cells-II. Reduction mechanism of CuO. *Electrochim. Acta* **30**, 1687–1692 (1985).

22. Benedeti, A. V., Sumodjo, P. T. A., Nobe, K., Cabot, P. L. & Proud, W. G. Electrochemical studies of copper, copper-aluminium and copper-aluminium-silver alloys: Impedance results in 0.5M NaCl. *Electrochim. Acta* **40**, 2657–2668 (1995).

23. Chen, W., Zhang, H., Ma, Z., Yang, B. & Li, Z. High electrochemical performance and lithiation-delithiation phase evolution in CuO thin films for Li-ion storage. *J. Mater. Chem. A* **3**, 14202–14209 (2015).

24. Malitesta, C., Rotunno, T., Sabbatini, L. & Zambonin, P. G. Insight into the intercalation problem of the Li/CuO cell by analytical electron spectroscopies. *J. Chem. Soc. Faraday Trans.* **86**, 3607–3611 (1990).

25. Yamakawa, N., Jiang, M. & Grey, C. P. Investigation of the conversion reaction mechanisms for binarycopper(ii) compounds by solid-state nmr spectroscopy and X-ray diffraction. *Chem. Mater.* **21**, 3162–3176 (2009).

26. An, S. J. *et al.* The state of understanding of the lithium-ion-battery graphite solid electrolyte interphase (SEI) and its relationship to formation cycling. *Carbon N. Y.* **105**, 52–76 (2016).

27. Assegie, A. A., Cheng, J. H., Kuo, L. M., Su, W. N. & Hwang, B. J. Polyethylene oxide film coating enhances lithium cycling efficiency of an anode-free lithium-metal battery. *Nanoscale* **10**, 6125–6138 (2018).

28. Martin, L., Martinez, H., Poinot, D., Pecquenard, B. & Le Cras, F. Direct observation of important morphology and composition changes at the surface of the CuO conversion material in lithium batteries. *J. Power Sources* **248**, 861–873 (2014).

29. Chavez, K. L. & Hess, D. W. A Novel Method of Etching Copper Oxide Using Acetic

Acid. *J. Electrochem. Soc.* **148**, 640–643 (2001).

30. Pecher, O., Carretero-Gonzalez, J., Griffith, K. J. & Grey, C. P. Materials' methods: NMR in battery research. *Chem. Mater.* **29**, 213–242 (2017).

31. Ross Macdonald, E. B. *Fundamentals of Impedance Spectroscopy*.

32. Diard, Jean-Paul & Le Gorrec, Bernard & Montella, C. *Handbook of Electrochemical Impedance Spectroscopy CIRCUITS made of RESISTORS and CAPACITORS.* (2007). doi:10.13140/RG.2.2.25393.12641.

33. IRVINE, J. T. S., SINCLAIR, D. C. & WEST, A. R. ChemInform Abstract: Electroceramics: Characterization by Impedance Spectroscopy. *ChemInform* **21**, 132–138 (2016).

34. Balbuena, P. B. *Lithium-Ion Batteries Solid-Electrolyte Interphase*. (Imperial College Press, 2004).

35. Omenya, F. *et al.* Intrinsic Challenges to the Electrochemical Reversibility of the High Energy Density Copper(II) Fluoride Cathode Material. *ACS Appl. Energy Mater.* **2**, 5243–5253 (2019).

36. Martin, L., Martinez, H., Poinot, D., Pecquenard, B. & Le Cras, F. Comprehensive X-ray photoelectron spectroscopy study of the conversion reaction mechanism of CuO in lithiated thin film electrodes. *J. Phys. Chem. C* **117**, 4421–4430 (2013).

37. Biesinger, M. C. Advanced analysis of copper X-ray photoelectron spectra. *Surf. Interface Anal.* **49**, 1325–1334 (2017).

38. Campion, C. L., Li, W. & Lucht, B. L. Thermal decomposition of LiPF 6-based electrolytes for lithium-ion batteries. *J. Electrochem. Soc.* **152**, 2327–2334 (2005).

39. Wiemers-Meyer, S., Jeremias, S., Winter, M. & Nowak, S. Influence of Battery Cell Components and Water on the Thermal and Chemical Stability of LiPF6 Based Lithium Ion Battery Electrolytes. *Electrochim. Acta* **222**, 1267–1271 (2016).

40. Meyer, B. M., Leifer, N., Sakamoto, S., Greenbaum, S. G. & Grey, C. P. High Field Multinuclear NMR Investigation of the SEI Layer in Lithium Rechargeable Batteries. 145–148 (2005) doi:10.1149/1.1854117.

41. Plakhotnyk, A. V., Ernst, L. & Schmutzler, R. Hydrolysis in the system LiPF 6 - Propylene carbonate - Dimethyl carbonate - H 2O. *J. Fluor. Chem.* **126**, 27–31 (2005).

42. Breuer, S., Pregartner, V., Lunghammer, S. & Wilkening, H. M. R. Dispersed Solid Conductors: Fast Interfacial Li-Ion Dynamics in Nanostructured LiF and LiF γ-Al2O3 Composites. *J. Phys. Chem. C* **123**, 5222–5230 (2019).

43. Huff, L. A. *et al.* Identification of Li-Ion Battery SEI Compounds through 7Li and 13C Solid-State MAS NMR Spectroscopy and MALDI-TOF Mass Spectrometry. *ACS Appl. Mater. Interfaces* **8**, 371–380 (2016).

44. Schurko, R. W. Ultra-wideline solid-state NMR spectroscopy. *Acc. Chem. Res.* **46**, 1985–1995 (2013).

45. KNIGHT, W. D. Nuclear Magnetic Resonance Shift in Metals. *Phys. Rev.* **76**, 1259 (1949).

46. Trease, N. M., Zhou, L., Chang, H. J., Zhu, B. Y. & Grey, C. P. In situ NMR of lithium ion batteries: Bulk susceptibility effects and practical considerations. *Solid State Nucl. Magn. Reson.* **42**, 62–70 (2012).

47. Yao, K. P. C. *et al.* Thermal stability of Li2O2 and Li2O for li-air batteries: In situ XRD and XPS studies. *J. Electrochem. Soc.* **160**, 824–831 (2013).

48. Svintsitskiy, D. A., Slavinskaya, E. M., Kardash, T. Y., Avdeev, V. I. & Senkovskiy, B. V. Applied Catalysis A : General Low-temperature catalytic CO oxidation over mixed silver – copper. *Appl. Catal., A* **510**, 64–73 (2016).

49. Nücker, N., Fink, J., Fuggle, J. C., Durham, P. J. & Temmerman, W. M. Evidence for holes on oxygen sites in the high-Tc superconductors La2-xSrxCuO4 and YBa2Cu3O7-y. *Phys. Rev. B* **37**, 5158–5163 (1988).

50. Tanaka, S., Taniguchi, M. & Tanigawa, H. XPS and UPS studies on electronic structure of Li2O. *J. Nucl. Mater.* **283**–**287**, 1405–1408 (2000).

51. Zatsepin, D. A. *et al.* Valence states of copper ions and electronic structure of LiCu2O2. *Phys. Rev. B* **57**, 4377–4381 (1998).

52. Strmcnik, D. *et al.* Electrocatalytic transformation of HF impurity to H2 and LiF in lithium-ion batteries. *Nat. Catal.* **1**, 255–262 (2018).

53. Solchenbach, S., Metzger, M., Egawa, M., Beyer, H. & Gasteiger, H. A. Quantification of PF5 and POF3 from side reactions of LiPF6 in li-ion batteries. *J. Electrochem. Soc.* **165**, A3022–A3028 (2018).

54. Aurbach, D., Markovsky, B., Shechter, A., Ein-Eli, Y. & Cohen, H. A comparative study of synthetic graphite and Li electrodes in electrolyte solutions based on ethylene carbonate-Dimethyl carbonate mixtures. *J. Electrochem. Soc.* **143**, 3809–3820 (1996).

55. Rinkel, B., Hall, D. S., Temprano, I. & Grey, C. P. Electrolyte oxidation pathways in lithium-ion batteries. *J. Am. Chem. Soc.* (2020) doi:10.1021/jacs.0c06363.

56. Clément, R. J., Kitchaev, D., Lee, J. & Gerbrand Ceder. Short-Range Order and Unusual Modes of Nickel Redox in a Fluorine-Substituted Disordered Rocksalt Oxide Lithium-Ion Cathode. *Chem. Mater.* **30**, 6945–6956 (2018).

57. Co, L. *et al.* Surface Chemistry Dependence on Aluminum Doping in Ni-rich. 1–12 (2019) doi:10.1038/s41598-019-53932-6.

58. Scholz, G., Stosiek, C., Noack, J. & Kemnitz, E. Local fluorine environments in nanoscopic magnesium hydr(oxide) fluorides studied by 19F MAS NMR. *J. Fluor. Chem.* **132**, 1079–1085 (2011).

59. T.G.Stoebe. Influence of OH- ions on infrared absorption and ionic conductivity in lithium fluoride crystals. *J. Phys. Chnn. Solid Fergamon* **28**, 1375–1382 (1967).

60. Biesinger, M. C., Hart, B. R., Polack, R., Kobe, B. A. & Smart, R. S. C. Analysis of mineral surface chemistry in flotation separation using imaging XPS. *Miner. Eng.* **20**,

152–162 (2007).

61. Biesinger, M. C., Lau, L. W. M., Gerson, A. R. & Smart, R. S. C. Resolving surface chemical states in XPS analysis of first row transition metals, oxides and hydroxides: Sc, Ti, V, Cu and Zn. *Appl. Surf. Sci.* **257**, 887–898 (2010).

62. Metzger, M., Strehle, B., Solchenbach, S. & Gasteiger, H. A. Hydrolysis of Ethylene Carbonate with Water and Hydroxide under Battery Operating Conditions. *J. Electrochem. Soc.* **163**, A1219–A1225 (2016).

63. Tian, F., Radin, M. D. & Siegel, D. J. Enhanced charge transport in amorphous Li2O2. *Chem. Mater.* **26**, 2952–2959 (2014).

64. Gileadi, E. *Electrode Kinetics for and Materials Scientists*. *VCH* (1993).

65. Gerbig, O., Merkle, R. & Maier, J. Electron and ion transport in Li2O2. *Adv. Mater.* **25**, 3129–3133 (2013).

66. McShane, E. J. *et al.* Quantification of Inactive Lithium and Solid-Electrolyte Interphase Species on Graphite Electrodes after Fast Charging. *ACS Energy Lett.* **5**, 2045–2051 (2020).

67. Tian, N., Hua, C., Wang, Z. & Chen, L. Reversible reduction of Li2CO3. 14173–14177 (2015) doi:10.1039/c5ta02499d.

68. Shao, L. *et al.* Preparation and characterization of basic carbonates as novel anode materials for lithium-ion batteries. *Ceram. Int.* **40**, 3105–3116 (2014).

69. Leon, J. J. D. *et al.* Reflectometry − Ellipsometry Reveals Thickness, Growth Rate, and Phase Composition in Oxidation of Copper. *ACS Appl. Mater. Interfaces* (2016) doi:10.1021/acsami.6b06626.

70. Wang, E., Dey, S., Liu, T., Menkin, S. & Grey, C. P. Effects of Atmospheric Gases on Li Metal Cyclability and Solid-Electrolyte Interphase Formation. *ACS Energy Lett.* 1088–1094 (2020) doi:10.1021/acsenergylett.0c00257.

71. Irvine, B. J. T. S., Sinclair, D. C. & West, A. R. <Electroceramics Characterisation by impedance sepctroscopy.pdf>. **2**, 132–138 (1990).

72. Eshkenazy, V. THE ROLE OF SEI IN LITHIUM AND LITHIUM ION BATTERIES E. PELED, D. GOLODNITSKY, G. ARDEL, C. MENACHEM, D. BAR TOW AND V. ESHKENAZY School of Chemistry, Tel Aviv University, Tel Aviv 69978, Israel. **393**, 209–221 (2020).

73. Campion, C. L., Li, W. & Lucht, B. L. Thermal Decomposition of LiPF 6 -Based Electrolytes for Lithium-Ion Batteries. *J. Electrochem. Soc.* **152**, A2327–A2334 (2005).

74. Grey, C. P. & Corbin, D. R. 19F and 27Al MAS NMR study of the dehydrofluorination reaction of hydrofluorocarbon-134 over basic faujasite zeolites. *J. Phys. Chem.* **99**, 16821–16823 (1995).

75. Wiemers-Meyer, S., Winter, M. & Nowak, S. Mechanistic insights into lithium ion battery electrolyte degradation-a quantitative NMR study. *Phys. Chem. Chem. Phys.*

18, 26595–26601 (2016).

76. Shenderovich, I. G. *et al.* Low-temperature NMR studies of the structure and dynamics of a novel series of acid-base complexes of HF with collidine exhibiting scalar couplings across hydrogen bonds. *J. Am. Chem. Soc.* **125**, 11710–11720 (2003).

77. Magnetic, N. & Studies, R. of Ion. 1878–1883 (1977).

78. Burkstrand, J. M. Unusual core level spectra of copper on polystyrene. *Surf. Sci.* **78**, 513–517 (1978).

79. Notes, S. & Kotzur, D. Influence of the Skin Effect on the Bloch Decay in Metals. *phys stat. sol.* **25**, (1972).

80. Ilott, A. J. & Jerschow, A. Super-resolution Surface Microscopy of Conductors using Magnetic Resonance. *Sci. Rep.* **7**, 1–7 (2017).

81. Kittel, C. Introduction to Solid State Physics, 8th edition. *Wiley Sons, New York, NY* (2004).

82. Lide, D. R. CRC Handbook of Chemistry and Physics, 84th Edition, 2003-2004. *Handb. Chem. Phys.* (2003) doi:10.1136/oem.53.7.504.

83. Gardam, G. E. The evaluation of throwing power in electrodeposition. *Trans. Faraday Soc.* **34**, 698–711 (1938).